Master's thesis

NTNU
Norwegian University of Science and Technology
Faculty of Natural Sciences
Department of Physics

Ida Due-Sørensen

Rapid carrier lifetime degradation and regeneration in high-performance multicrystalline silicon wafers

Master's thesis in Applied Physics and Mathematics
Supervisor: Jon Andreas Støvneng, Rune Søndenå (IFE)
July 2020

NTNU
Norwegian University of
Science and Technology

IFE

NTNU
Norwegian University of
Science and Technology

Rapid carrier lifetime degradation and regeneration in high-performance multicrystalline silicon wafers

Ida Due-Sørensen

Master's thesis in Applied Physics and Mathematics
Submission date: July 2020
Supervisor: Jon Andreas Støvneng
Co-supervisor: Rune Søndenå (IFE)

Norwegian University of Science and Technology
Department of Physics

Abstract

The aim of this thesis is to gain a further understanding of the degradation in *p*-type high-performance multicrystalline silicon (HPMC-Si) using quasi-steady state photoconductance (QSSPC) and photoluminescence-imaging (PL-I) characterization techniques to contribute to the development of robust engineering solutions to improve the efficiency of passivated emitter and rear contact (PERC) modules on multicrystalline silicon (mc-Si) substrates. This solar cell architecture has a higher efficiency potential as compared to the previous industry-standard device. However, PERC modules are subjected to a degradation process termed light and elevated temperature-induced degradation (LeTID) which can cause detrimental efficiency losses in the field. Despite the significant research effort, the root cause of the degradation is still unknown, impeding the progress of higher-efficiency PERC modules on *p*-type HPMC-Si substrates. The quality of the silicon wafer has a direct impact on the performance of a solar cell, and it is limited by impurities, crystal defects and their interactions. A good indication of the efficiency of the solar cell is the minority carrier lifetime. In this work, LeTID and the following regeneration of the carrier lifetime in industry-standard *p*-type HPMC-Si wafers were studied under illumination (0.5–3 suns) at elevated temperatures (100–300 °C). The results show that both the applied illumination and temperature can substantially alter the reaction rates. Additionally, a 20 min pre-dark anneal (DA) step at 300 °C appears to reduce the degradation extent and slow the reaction rates. Furthermore, the completeness of the regeneration is found to be noticeably reduced with increasing temperatures. The Arrhenius degradation and regeneration activation energies were found to be in the range 0.64–0.94 eV and 0.77–0.97 eV, respectively. Lastly, a spatial evaluation found the reaction rates to be dependent on the initial lifetime, while no obvious trend was found for the activation energies.

Sammendrag

Målet med denne masteroppgaven er å øke forståelsen av degradering i *p*-type høyytelse multikrystallinsk silisium (HPMC-Si) ved bruk av karakteriseringsteknikkene kvasi-likevektstilstand fotokonduktans (QSSPC) og fotoluminescens-avbildning (PL-I) med det formål å bidra til utviklingen av robuste ingeniørløsninger for å forbedre effektiviteten til de passiverte emitter- og baksidekontakt (PERC)-modulene på multikrystallinske silisium (mc-Si)-substrater. Denne solcellearkitekturen har et høyere effektivitetspotensial enn den tidligere industristandarden, men er imidlertid utsatt for en degraderingsprosess kalt lys- og forhøyet temperaturindusert degradering (LeTID) som kan forårsake ugunstige effektivitetstap. Til tross for en betydelig forskningsinnsats, er årsaken til degraderingen fortsatt ukjent, noe som hindrer fremgangen i utviklingen av høyere effektivitets PERC-moduler på *p*-type HPMC-Si-substrater. Kvaliteten på silisiumwaferen har en direkte innvirkning på ytelsen til solcellen, og den er begrenset av urenheter, krystalldefekter og deres interaksjoner. En god indikasjon på solcellens effektivitet er minoritets ladningsbærerens levetid. I dette arbeidet ble LeTID og påfølgende regenerering av ladningsbærerens levetid i industristandard *p*-type HPMC-Si-wafere studert under belysning (0,5–3 soler) ved høye temperaturer (100–300 °C). Resultatene viser at både den påførte belysningen og temperaturen kan endre reaksjonshastighetene vesentlig. I tillegg ser det ut til at 20 min oppvarming ved 300 °C i mørket før belysning ved høye temperaturer minsker degraderingsgraden og reduserer reaksjonshastighetene. Videre er fullstendigheten av regenereringen merkbart redusert med økende temperaturer. Arrhenius-degraderings- og regenereringsaktiveringsenergiene ble funnet å være mellom henholdsvis 0,64–0,94 eV og 0,77–0,97 eV. Til slutt fant en romlig evaluering at reaksjonshastighetene er avhengige av initial levetid, mens ingen åpenbar trend ble funnet for aktiveringsenergiene.

Preface

This master's thesis completes my Master of Science degree in Applied Physics and Mathematics at the Norwegian University of Science and Technology (NTNU). The thesis is written in co-operation with the Institute for Energy Technology (IFE), and it succeeds my specialization project report "Material quality investigation of high-performance multicrystalline silicon by grain size and carrier lifetime measurements" from the fall of 2019. In that project, we investigated the effect of seeding on the grain structure and the minority carrier lifetime in compensated high-performance multicrystalline silicon (HPMC-Si) wafers.

For this thesis work, the focus is moved to accelerated lifetime degradation and regeneration in p-type HPMC-Si wafers. Some of the theory and experimental details sections in this thesis are partly or entirely based on their respective sections from the specialization project report. These include Section 2.1, Section 2.2, Section 2.3, Section 3.1.2.1 and Section 3.2.

Measurements, characterization and analysis thereof have been carried out by yours truly, while the initial processing of the wafers was performed in close collaboration with my supervisor, Rune Søndenå, due to safety reasons.

The thesis is intended for an audience with a background in physics at the master level with limited knowledge of the field of photovoltaics.

Ida Due-Sørensen
July 2020
Kjeller

Acknowledgements

First, I would like to express how fortunate I feel for being given the opportunity to write my master's thesis in collaboration with competent researchers in such an appreciative environment as IFE. In particular, I am grateful the lab could stay open during the COVID-19 outbreak, which allowed my experimental work to continue with only minimal delays.

I would like to pay my special regards to my supervisor, Rune Søndenå, for the guidance, encouragement and advice he has provided throughout my time at IFE. He consistently allowed this thesis to be my own work but steered me in the right direction whenever he thought I needed it. The door to Rune's office was always open whenever I had a question about my lab work or writing, and I probably should have used Rune's knowledge even more.

Thanks to the wafer group for valuable discussions during Monday meetings. Special thanks to Guro Marie Wyller for always being available to help me sort my thoughts, for short pep talks, feedbacks and fruitful discussions on LeTID kinetics and spatial dependence. A big thanks to Halvard Haug for taking me in at IFE and even with a busy schedule finding time to discuss ideas and concepts and explain MATLAB-scripts during my specialization project work.

Next, I would like to thank my supervisor at NTNU, Jon Andreas Støvneng, for help with all formalities, optimism and valuable feedback in the writing process.

I must express my appreciation to Kristoffer Skuland for help proofreading this thesis. I am gratefully indebted to him for his valuable comments. Thanks also to my go-to guy for statistical questions, Silius Mortensønn Vandeskog.

Completing this master's degree would have been possible, but all the more difficult were it not for the social, cultural, applicable and professional rewards of the extracurricular student life in Trondheim. I would like to show my greatest appreciation to the student organization Nabla for facilitating friendship which I am sure will last a lifetime, and for letting me evolve my creative side as the editor of *Nabladet*.

I would also like to thank my boyfriend, Kristoffer, for being patient in my absence this semester, for all the cheers and love, and for always believing in me.

Finally, I must express my very profound gratitude to my family for giving me the opportunity to pursue my interests and for providing me with unfailing support and patience throughout my years of study and through the process of researching and writing this thesis. This accomplishment would not have been possible without them.

Thank you.

Contents

List of Figures

List of Tables

Abbreviations

Notation	Description
AC	As-Cut
Al-BSF	Aluminum Back-Surface Field
ARC	Anti-Reflection Coating
B	Boron
B–O	Boron–Oxygen
c-Si	Crystalline Silicon
CAGR	Compound Annual Growth Rate
CB	Conduction Band
CCD	Charge-Coupled Device
CID	Carrier-Induced Degradation
Cz	Czochralski
Cz-Si	Czochralski-Silicon
DA	Dark Anneal
ESS™	Elkem Solar Silicon™
Fe–B	Iron–Boron
FZ	Float-Zone
Ga	Gallium
HPMC	High-Performance Multicrystalline
HPMC-Si	High-Performance Multicrystalline Silicon
IFE	Institute for Energy Technology
LED	Light Emitting Diode
LeTID	Light and Elevated Temperature-Induced Degradation
LID	Light-induced degradation

Notation	Description
LS	Light Soak
mc-Si	Multicrystalline Silicon
MSE	Mean Squared Error
NDD	Normalized Defect Density
P	Phosphorus
PDG	Phosphorus Diffusion Gettered
PDGH	Phosphorus Diffusion Gettered and Hydrogenated
PECVD	Plasma-Enhanced Chemical Vapor Deposition
PERC	Passivated Emitter and Rear Contact
PL	Photoluminescence
PL-I	Photoluminescence-Imaging
ppmw	parts per million weight
PV	Photovoltaic
QSSPC	Quasi-Steady State Photoconductance
REDR	Recombination Enhanced Defect Reactions
SRD	Surface-Related Degradation
SRH	Shockley–Read–Hall
STC	Standard Test Conditions
VB	Valence Band

Physical Parameters and Constants

Notation	Description	Unit
B_{rad}	Radiative recombination coefficient	$\mathrm{cm^3s^{-1}}$
c	Speed of light	$\mathrm{ms^{-1}}$
C_0	Impurity concentration in the liquid	ppmw
C_{cal}	Calibration constant used for PL imaging	$\mathrm{cm^3s}$
C_{l}	Compensation level	
C_n	Auger coefficient	$\mathrm{cm^6s^{-1}}$
C_p	Auger coefficient	$\mathrm{cm^6s^{-1}}$
C_{s}	Impurity concentration in the solid	ppmw
r_{deg}	Degradation rate	$\mathrm{s^{-1}}$
E_{C}	Conduction band edge	eV
E_{G}	Band gap	eV
$E_{\mathrm{deg/reg}}$	Degradation/regeration activation energy	eV
E	Energy	eV
E_{t}	Trap state energy	eV
E_{V}	Valence band edge	eV
G	Carrier generation rate	$\mathrm{cm^{-3}s^{-1}}$
h	Planck's constant	$\mathrm{m^2\,kg\,s^{-1}}$
I_{PL}	Detected PL intensity	counts/s
J	Current density	$\mathrm{A/m^2}$
k	Boltzmann constant	eV/K
k	Wavevector	$\mathrm{nm^{-1}}$
k_{eff}	Effective segregation coefficient	

Notation	Description	Unit
λ	Wavelength	nm
μ_{n}	Electron mobility	$\mathrm{cm}^2/\mathrm{Vs}$
μ_{p}	Hole mobility	$\mathrm{cm}^2/\mathrm{Vs}$
Δn	Exess electron concentration, injection level	cm^{-3}
n	Electron concentration in the conduction band	cm^{-3}
n_0	Electron concentration at thermal equilibrium	cm^{-3}
n_1	Statistical parameter for SRH recombination	cm^{-3}
N_{A}	Acceptor doping concentration	cm^{-3}
N_{D}	Donor doping concentration	cm^{-3}
NDD	Normalized defect density	s^{-1}
n_{i}	Intrinsic carrier density at thermal equilibrium	cm^{-3}
N_{t}	Trap density	cm^{-3}
OC	Optical constant for QSSPC measurements	
Δp	Exess hole concentration, injection level	cm^{-3}
p	Hole concentration in the valence band	cm^{-3}
p_0	Hole concentration at thermal equilibrium	cm^{-3}
p_1	Statistical parameter for SRH recombination	cm^{-3}
Φ	Photon flux	$\mathrm{cm}^{-2}\mathrm{s}^{-1}$
Φ_{ph}	Excitation photon flux	$\mathrm{cm}^{-2}\mathrm{s}^{-1}$
Φ_{PL}	Rate of photoluminescence emission	s^{-1}
p_{i}	Intrinsic carrier density at thermal equilibrium	cm^{-3}
p	Power density	mWcm^{-2}
q	Elementary charge	C
r_{reg}	Regeneration rate	s^{-1}
R_{sheet}	Sheet resistance	$\Omega/\square$
$\Delta\sigma$	Excess photoconductivity	S
T	Temperature	K
τ	Recombination lifetime	s
τ_{Aug}	Auger lifetime	s
τ_{bulk}	Bulk lifetime	s
τ_{eff}	Effective lifetime	s
τ_{n0}	Capture time constants for electrons	s
τ_{p0}	Capture time constants for holes	s
τ_{rad}	Radiative lifetime	s
τ_{SRH}	SRH lifetime	s
τ_{surf}	Surface lifetime	s

Notation	Description	Unit
U	Rate of recombination	$\mathrm{cm}^{-3}\mathrm{s}^{-1}$
U_{Aug}	Rate of Auger recombination	$\mathrm{cm}^{-3}\mathrm{s}^{-1}$
U_{eff}	Effective recombination rate	$\mathrm{cm}^{-3}\mathrm{s}^{-1}$
U_{rad}	Rate of radiative recombination	$\mathrm{cm}^{-3}\mathrm{s}^{-1}$
U_{SRH}	Rate of SRH recombination	$\mathrm{cm}^{-3}\mathrm{s}^{-1}$
U_{surf}	Rate of surface recombination	$\mathrm{cm}^{-3}\mathrm{s}^{-1}$
v_{th}	Carrier thermal velocity	cm/s

Chapter 1

Introduction

Solar energy is free, abundant and widely distributed – available over the entire globe and to every person in the world. This is why solar energy is the ultimate source of power and presented as part of the solution to ensure access to affordable, reliable, sustainable and modern energy for all in the UN Sustainable Development Goals [1]. The photovoltaic (PV) effect is the most elegant way to take advantage of the energy from the sun. Light shining on PV solar cells, is converted directly to electricity with only a minor impact on the environment. Photovoltaics is a fast-growing market, and from 2010 to 2018 the compound annual growth rate (CAGR) of PV installations was 36.8 % [2].

The fundamental challenge for the PV industry, as it continues to grow, is to improve efficiency while further decreasing the overall cost of electricity production and the carbon footprint of solar energy. Passivated emitter and rear contact (PERC) is a solar cell architecture that has higher efficiency potential as compared to the previous industry-standard device, the aluminum back-surface field (Al-BSF). Even if there are more steps in the PERC manufacturing process, the gain in efficiency enables costs to decrease.

The PERC cell structure is subjected to a degradation process termed light and elevated temperature-induced degradation (LeTID), which can cause relative efficiency degradation of about 6–12 % in the field [3–9]. Extended exposure to the conditions that induce degradation leads to natural recovery in performance. The recovery may take many years under field conditions, making this degradation a potential limiting factor for the development of p-type multicrystalline silicon (mc-Si) high-efficiency PERC solar cells. Research to date has not succeeded in determining the root cause of LeTID, and this uncertainty impedes progress in the development of robust engineering solutions that can be applied to both current and future cell architectures.

Cell concepts with diffused and passivated p–n junctions and passivated rear sides had a market share of more than 60 % in 2019 and are predicted to dominate

the market this decade [10]. Currently, high-performance multicrystalline silicon (HPMC-Si) faces strong competition from monocrystalline silicon wafers. To reclaim the market shares, further improvements are needed. Mitigating or avoiding the detrimental LeTID effect is therefore vital. Enhancement of *p*-type mc-Si material performance can be obtained by gallium co-doping due to improved doping homogeneity. Additionally, it has recently been demonstrated that boron–gallium co-doping can effectively reduce the light-induced degradation (LID) extent [11]. Increased use of gallium as a dopant has emerged in the industry. Out of boron-doped mc-Si material, the market share of co-doping with gallium and compensation with phosphorus was about 40 % in 2019 and is predicted to increase fast to 100 % by 2030 [10]. For this reason, studies of LeTID in boron–gallium co-doped industry-standard HPMC-Si wafers are highly relevant today.

A good indication of the efficiency of the solar cell is the minority carrier lifetime, the key parameter determining the material quality of crystalline silicon (c-Si) wafers for solar cells. Furthermore, the bulk lifetime is known to be the primary parameter affected by LeTID [4]. Thus, understanding the lifetime degradation and regeneration – and how to mitigate the degradation – is crucial to the improvement of efficiency.

This master's thesis presents a study on the minority carrier lifetime degradation and regeneration due to LeTID in boron–gallium co-doped, compensated HPMC-Si wafers. In the first part of this thesis, the main focus is placed on gaining a further understanding of the complex LeTID defect mitigation. The purpose is to contribute to finding an industrially relevant post-process for LeTID mitigation. In the second part, we attempt to understand the root cause. Six objectives were set. The objectives of the first part were to: (1) study the accelerated degradation and regeneration at 3 suns illumination and a range of temperatures, (2) investigate the impact of dark annealing prior to accelerated degradation and regeneration, (3) test the stability of regenerated wafers and ultimately (4) examine the reaction rates dependencies of the illumination intensity. The objectives of the second part were to: (5) extract the activation energy at different illumination intensities and (6) asses the spatial variations in LeTID behavior.

The thesis is divided into six chapters. In the present chapter, the master's thesis work is placed into a broader context, and a short motivation and goals for the work is given.

Chapter 2 provides the reader with the necessary theoretical background to apprehend the discussion in following chapters. Firstly, the basic operation of a solar cell is explained, and three steps in the process are introduced before the focus is shifted to recombination as one of the major factors limiting solar cell efficiency. The successive section introduces the material properties of compensated silicon. Lastly, a literature review of LeTID in mc-Si is presented.

Chapter 3 describes the sample preparation, the techniques used for lifetime characterization, the meaning of the unit "suns" in light-induced degradation (LID) experiments and the different treatment groups for LeTID investigations. In addi-

tion, a presentation of the model used to calculate degradation and regeneration rates and the procedure for extracting activation energies is given.

The first part of Chapter 4 focuses on gaining a further understanding of the complex LeTID defect mitigation. Section 4.1.1 presents the accelerated degradation and regeneration under 3 suns results. The section includes the impact of DA and stability results. Section 4.2.1 addresses the reaction rates dependency of illumination and temperature. In the second part of Chapter 4, we attempt to understand the root cause of LeTID. Section 4.2.2 presents and discusses the estimated activation energies. Finally, in Section 4.3, the spatial LeTID results are presented and discussed.

In Chapter 5 some concluding remarks on the master's thesis work are given, and Chapter 6 presents suggestions to further work.

Chapter 2

Theory and Literature Review

In this chapter, the basic operation of a solar cell, carrier generation, recombination mechanisms and properties of compensated silicon are presented. This is done to provide the reader with the necessary theoretical background for the measurements, calculations and discussions of the later chapters. We refer the reader to one of several good textbooks on the topic [12–14] for a more thorough review of the concepts. Finally, the status of LeTID research is reviewed.

2.1 Basic Solar Cell Operation

Solar cells are based on the PV effect, i.e., the generation of a potential difference at the junction of two different semiconducting materials in response to electromagnetic radiation [15]. The direct conversion of sunlight into electricity can be divided into three basic processes:

1. Generation of charge carriers due to the absorption of photons

Absorption of a photon in a semiconductor means that its energy is used to excite an electron from an initial energy level E_i to a higher energy level E_f, as shown in Figure 2.1.1a [15]. The semiconductor has two bands of energies which the valence electrons can possess: the valence band (VB) and the conduction band (CB). In other words, the electrons can populate energy levels below the VB edge, E_V, and above the CB edge, E_C. A band-gap, $E_\mathrm{G} = E_\mathrm{C} - E_\mathrm{V}$, separates the two bands. This is the range of energies the electrons are not allowed to populate. Sunlight consists of a certain fraction of photons with energy larger than the band-gap energy. These photons may excite electrons in a semiconductor to the CB where they are free to move [16]. An excited electron in the CB leaves an excited hole in the VB.

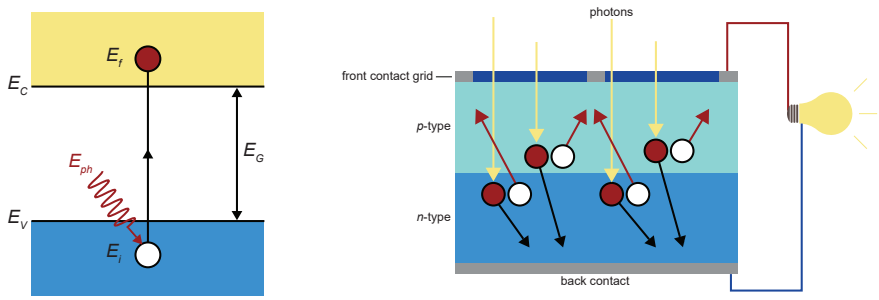

(a) **(b)**

Figure 2.1.1: **(a)** Exciting an electron from E_i to E_f. **(b)** Basic solar cell concept which illustrates the separation of charge carriers by the electric field created by a p–n junction. The carriers are subsequently collected at the front and back contacts.

2. Separation of the generated charge carriers

Generally, the excited electron will fall back to the VB and recombine with the excited hole. When the carriers recombine, the light-generated electron–hole pair is lost and no current or power can be generated. In order to use the energy stored in the electron–hole pair for performing electric work, the excited electrons and holes must be separated and directed in opposite directions to produce a net current [17]. The design has to be such that the electrons and holes are spatially separated before they recombine, i.e., the time it requires to spatially separate the charge carriers must be shorter than their lifetime [15].

Doping is, to put it briefly, one way to control the conductivity in a semiconductor by adding a finite amount of impurity elements. Silicon is a four-valent element; ideally each silicon atom bonds with four other atoms to complete the electron octet. Elements from groups III and V are used for doping. The most commonly used dopant in the growth of silicon ingots for PV applications is boron. Boron is a three-valent element and thereby creates mobile holes, which in this case, are the majority charge carriers. When allowing the hole to move by accepting an electron from a neighboring atom, boron acts as an acceptor. This type of conduction by positive hole transport is called p-type. Phosphorus, a five-valent element, is the most common dopant when free electrons are needed. In this case, phosphorus acts as a donor. Doping with phosphorus increases the conductivity of the semiconductor by increasing the negatively charged carrier density, hence silicon doped with phosphorus is called n-type, and the electrons are the majority charge carriers in such materials [18]. The type of carriers with lower concentration are called the *minority carriers*.

In most solar cells, the separation of generated charge carriers is accomplished by joining two layers of semiconductor materials with different doping to form a p–n junction (Figure 2.1.1b). This junction causes excess holes from the p-type material to diffuse to the n-type side and excess electrons in the n-type material

to diffuse to the p-type side. Consequently, the acceptor atoms in the p-type layer and the donor atoms in the n-type layer ionized, which results in an electric field, E, forming between the negative ion cores in the p-type material and positive ion cores in the n-type material. This region is called the *depletion region* since the electric field quickly sweeps free carriers out, and hence the region is depleted of free carriers [19].

3. Collection of the generated charge carriers

Ultimately, the charge carriers need to be extracted to an external load [18]. When contacts have been applied on each side of the junction, the device can now accumulate power when light shines on it. The initial energy of the electron–hole pair is now converted to electric energy. After passing through the circuit, the electrons will recombine with holes.

As discussed above, the PV effect requires three steps. Each of these steps can be sources of loss in solar cell efficiency, and thus they create multiple challenges for solar cell design and manufacturing, which makes all steps important fields of research. This master's thesis focuses on the mitigation and root cause of LeTID. A discussion of recombination mechanisms is required to understand how this is related to solar cell operation.

2.2 Carrier Generation and Recombination Mechanisms

Carrier recombination is one of the major factors limiting solar cell efficiency. The generated electron–hole pair may recombine before it can be collected and contribute to the current, by any number of removal mechanisms. Several different recombination mechanisms can be important, contrary to generation where one mechanism is dominant.

There is a distinction between *intrinsic* and material quality-related recombination processes. The intrinsic mechanisms are inherent to the existence of separated energy bands in the material and are caused by band-to-band transitions, whereas the material quality-related recombination is dependent on the concentration of defects and imperfection present.

In experiments, the recombination lifetime, τ, is measured. It is related to the recombination rate per volume, U, by

$$\tau \equiv \frac{\Delta n}{U}, \tag{2.1}$$

where Δn is the excess minority carrier concentration often referred to as the *injection level*.

2.2.1 Bulk recombination mechanisms

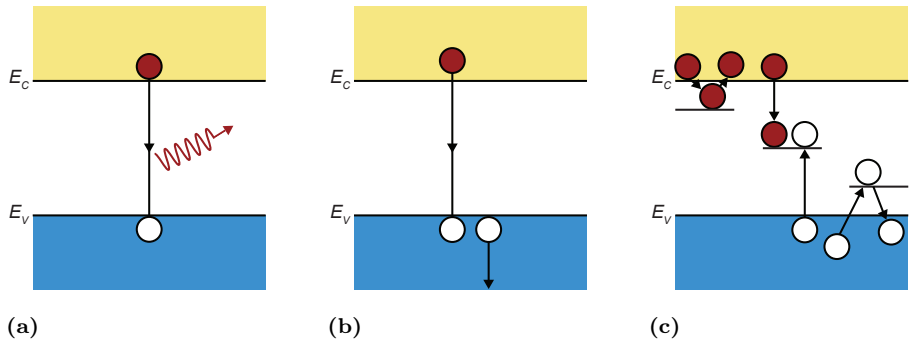

Figure 2.2.1: Schematic illustration of bulk recombination mechanisms. **(a)** Radiative band-to-band. **(b)** Auger recombination with two holes involved. **(c)** SRH recombination in a single-electron trap state. The illustration also shows the process of electron trapping and de-trapping close to the CB, and of analogous hole trapping and detrapping close to the VB.

2.2.1.1 Intrinsic recombination mechanisms

Radiative recombination

Radiative recombination is the exact opposite of the optical generation process. An electron–hole pair is annihilated, releasing a photon. The emitted photon has energy close to the band gap and is therefore only weakly absorbed. Figure 2.2.1a illustrates the process. The radiative recombination rate, U_{rad}, is proportional to $(np - {n_{\mathrm{i}}}^2)$,

$$U_{\mathrm{rad}} = B_{\mathrm{rad}}(np - {n_{\mathrm{i}}}^2), \tag{2.2}$$

where n is the electron concentration in the CB, p is the hole concentration in the VB, n_{i} is the intrinsic carrier concentration at thermal equilibrium and B_{rad} is a carrier density-independent and material-specific parameter called the radiative recombination coefficient. $B_{\mathrm{rad}} = 9.5 \cdot 10^{-15}\,\mathrm{cm^3s^{-1}}$ for Si at room temperature [20].

Assuming charge neutrality $\Delta n{=}\Delta p$, and using the expressions for the non-equilibrium carrier densities, $n{=}n_0{+}\Delta n$ and $p{=}p_0{+}\Delta n$, we may express U_{rad} as

$$U_{\mathrm{rad}} = \frac{\Delta n}{\tau_{\mathrm{rad}}}, \tag{2.3}$$

where

$$\tau_{\mathrm{rad}} = \frac{1}{B_{\mathrm{rad}}(p_0 + n_0 + \Delta n)} \tag{2.4}$$

is the minority carrier radiative lifetime.

Silicon is an indirect band gap semiconductor, which means that the top of the VB and the bottom of the CB do not coincide in E–k-space (k is the wavevector). Therefore, both the emission of a photon and a phonon are required to conserve momentum. As a result, the probability of radiative recombination is low and can usually be neglected. Recombination in silicon is dominated by the other recombination mechanisms.

Auger recombination

Auger recombination involves three carriers wherein an electron and a hole recombine and, consequently, transfer the excess energy to a CB electron or a VB hole [21]. Figure 2.2.1b illustrates the case where the excess energy is transferred to a hole. Just as for the radiative recombination, the recombination rate is given as the product of the concentrations of the involved carriers

$$U_{\mathrm{Aug}} = C_n(n^2p - {n_{\mathrm{i}}}^2 n_0) + C_p(np^2 - p_0{n_{\mathrm{i}}}^2) \approx C_n n^2 p + C_p n p^2, \tag{2.5}$$

where C_n and C_p are the Auger coefficients. Assuming a p-type material, the expressions for the Auger lifetime become

$$\tau_{\mathrm{Aug,LI}} = \frac{1}{C_p {N_{\mathrm{A}}}^2} \quad \text{and} \quad \tau_{\mathrm{Aug,HI}} = \frac{1}{(C_n + C_p)\Delta n^2}, \tag{2.6}$$

for low and high injection levels, respectively.

The Auger lifetime scales with the inverse of the majority carrier concentration squared and is hence most important at high carrier concentrations caused by heavy doping or high-level injection under concentrated sunlight. In silicon-based solar cells, Auger recombination limits the lifetime and ultimate efficiency for very high injection levels or heavily doped regions.

2.2.1.2 Recombination through defect levels

Recombination can occur in defect energy levels and does not occur in perfectly pure, undefected materials. The defect energy levels may greatly increase the recombination rate. This recombination mechanism is material quality-related. It is also referred to as Shockley–Read–Hall (SRH) recombination, as it was first investigated by Shockley and Read [22] and at the same time by Hall [23]. The SRH recombination is a two-step process: (1) First, an electron or a hole is trapped

in a defect energy level which is introduced through defects in the crystal lattice. These defects are either added, e.g., by intentionally doping the material, or they are unintentionally introduced. (2) In the case of a trapped electron, recombination occurs if a hole moves to the same defect energy level before the electron is thermally re-emitted into the CB. Figure 2.2.1c illustrates this process.

The distance of the introduced defect energy level determines the rate carriers move into the energy level. Hence, if the defect level is close to the CB edge, the electron is likely to be re-emitted to the CB edge rather than to recombine with a hole moving into the same energy level from the VB. Thus, defect energy states deep within the band gap are effective recombination centers.

The SRH recombination rate may be written as

$$U_{SRH} = \frac{np - {n_\mathrm{i}}^2}{\tau_{p0}(n + n_1) + \tau_{n0}(p + p_1)} \tag{2.7}$$

where the capture constant of holes or electrons are

$$\tau_{p_0/n_0} = \frac{1}{v_\mathrm{th}\sigma_{p/n}N_\mathrm{t}}, \tag{2.8}$$

and

$$n_1 = n_\mathrm{i}\exp\left(\frac{E_\mathrm{t} - E_\mathrm{i}}{kT}\right)\text{and} \quad p_1 = p_\mathrm{i}\exp\left(\frac{-(E_\mathrm{t} - E_\mathrm{i})}{kT}\right). \tag{2.9}$$

Here, σ_n and σ_p are the capture cross sections for electrons and holes, N_t is the trap density, E_t is the trap state energy, v_th is the carrier thermal velocity and kT is the product of the Boltzmann constant and the temperature.

Assuming charge neutrality $\Delta n{=}\Delta p$ and combining Equation (2.1) with Equation (2.7), we can write

$$\tau_\mathrm{SRH} = \frac{\tau_{p0}(n + n_1 + \Delta n) + \tau_{n0}(p + p_1) + \Delta n}{n_0 p_0 + \Delta n}. \tag{2.10}$$

From this expression, we can see that at low injection in a p-type material, the majority carriers will dominate, so that $\tau_\mathrm{SRH} \approx \tau_{n0}$. At high injections, $\tau_\mathrm{SRH} \approx \tau_{n0} + \tau_{p0}$.

2.2.2 Surface recombination

At the surface of a semiconductor sample, the periodicity of the crystal lattice is terminated. This discontinuity introduces a large number of dangling bonds caused

by partially bonded Si atoms at the surface. The dangling bonds cause energy states in the band gap, which results in very high recombination activity. It is possible to reduce the density of dangling bonds, and thereby the surface recombination, although it is an intrinsic mechanism. Such a reduction can be achieved by growing a passivation layer on top of the semiconductor which forms chemical bonds with the partially bonded Si atoms. One common way to passivate the surface is to thermally grow a layer of SiO_2 that saturates the unsaturated bindings and hence reduces the number of energy states in the band gap.

The lifetime of the material is dependent upon the concentration of minority carriers. Limiting the surface recombination leads to longer cell lifetimes by limiting the rate at which minority carriers are depleted.

2.2.3 Effective carrier lifetime

In a solar cell, the recombination mechanisms described above will typically occur simultaneously. By adding all the different recombination rates, we obtain the total recombination rate, U_{eff},

$$U_{\text{eff}} = U_{\text{rad}} + U_{\text{Aug}} + U_{\text{SRH}} + U_{\text{surf}} + U_{\text{other}}. \tag{2.11}$$

As we have seen, the recombination lifetime is inversely proportional to the recombination rate and can be found for each mechanism. Adding the different inverse lifetime contributions gives

$$\frac{1}{\tau_{\text{eff}}} = \underbrace{\frac{1}{\tau_{\text{rad}}} + \frac{1}{\tau_{\text{Aug}}}}_{\text{intrinsic}} + \frac{1}{\tau_{\text{SRH}}} + \frac{1}{\tau_{\text{surf}}} + \frac{1}{\tau_{\text{other}}} = \frac{1}{\tau_{\text{bulk}}} + \frac{1}{\tau_{\text{surf}}} + \frac{1}{\tau_{\text{other}}}. \tag{2.12}$$

In experiments, τ_{eff} is the measured value. As discussed above, some of the mechanisms are more important in Si and will thus dominate the measured value of τ_{eff}. Note that since τ_{eff} equals the inverse sum of its components, the total lifetime will be dominated by the recombination process with the lowest recombination lifetime. Figure 2.2.2 shows an example of the minority carrier lifetime with its components as a function of injection level.

Importance of minority carrier lifetime for the efficiency of a solar cell

Ideally, all the generated carriers in the solar cell are collected and extracted to an external load before they recombine within the cell. Energy output from the cell will be reduced by short carrier lifetimes (high recombination rates). Even though the absolute rate of recombination of the majority and minority charge carriers must equal, the density of majority charge carriers can be considered constant.

This is because the density of majority carriers is several orders of magnitude higher than the density of minority carriers. The density of minority carriers is, in contrast, highly impacted by recombination and is thus a key parameter for the energy conversion of the solar cell.

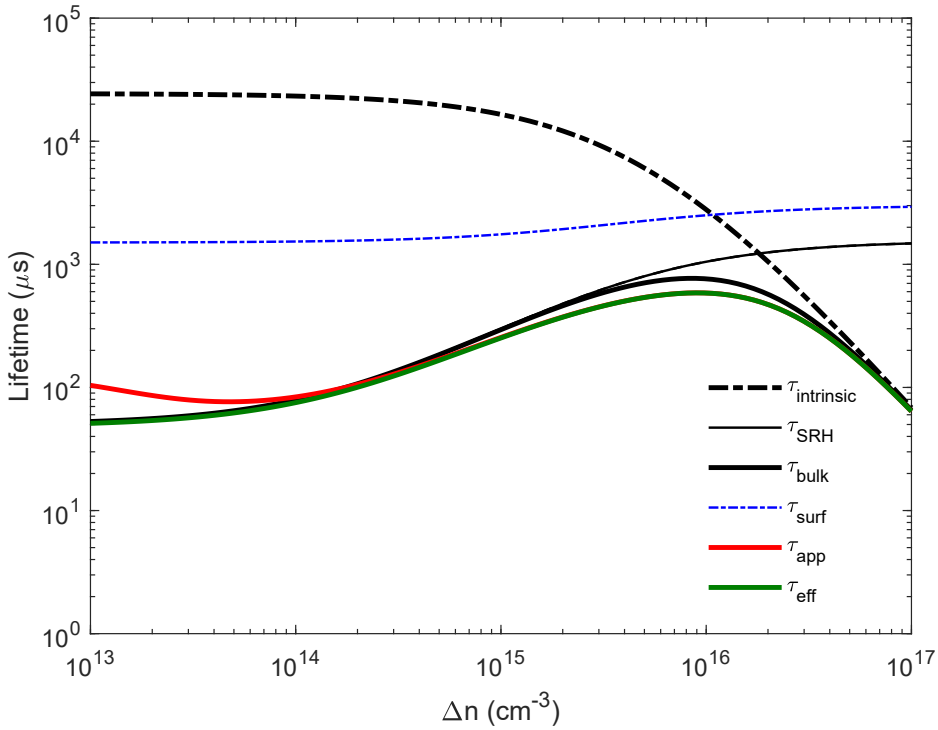

Figure 2.2.2: Example of the effective lifetime as a function of injection level for the described recombination mechanisms in Section 2.2. The effective lifetime, τ_{eff}, equals the inverse sum of its components, and it is thus limited by its smallest component. Also shown is the apparent lifetime, τ_{app}, due to trap states (described in Section 2.2.4).

2.2.4 Effect of trapping on lifetime measurements

A trap state is a state within a semiconductor that restricts the movement of a carrier and prevents its recombination with the carrier of opposite charge. The carrier may break free from the trap quickly, or it may remain trapped for an extended period. If the trap is created in the middle of the band gap by impurities, the probability of capturing an electron and a hole is similar, hence traps in the middle of the band gap act as recombination centers. Energy levels near the band edges have a higher probability of capturing either electrons or holes. For energy levels near the CB edge, the probability of capturing electrons is much higher than for capturing holes. Electrons trapped by these states are unlikely to recombine and do not reduce the minority carrier lifetime. Regardless, these shallow level

traps cause considerable problems with lifetime measurements.

Charge neutrality is always preserved, meaning that the trapped carrier has a mobile carrier of the opposite polarity associated with it. An electron in a shallow level trap has a mobile hole associated with it that increases the sample conductivity. Quasi-steady state photoconductance (QSSPC) is, as we will get back to in Section 3.2.1, one way to measure the carrier lifetime. The technique measures the conductivity of the sample to calculate the carrier concentration under steady state conditions as a measure of carrier lifetime. Thus, the increase in the conductivity due to the mobile hole is wrongly measured as a high lifetime in the material.

The traps fill first, so even with a low number of shallow traps, the traps dominate the QSSPC measurements at low injection levels. With an increased number of carriers generated by light, the percentage of carriers trapped is only a small fraction of the total, and the traps usually only have a minor effect. The number of trapped carriers is estimated to be constant with injection level and can thus be corrected for.

2.3 Compensated Silicon

2.3.1 The Elkem Solar process route

The metallurgical process route of REC Solar Norway (formerly Elkem Solar) for solar grade silicon feedstock production is based on the chemical route. It is a five-step process, including the creation of metallurgical-grade silicon, purification steps such as slag treatment and leaching, directional solidification and post-treatment.

In the first purification step, molten metallurgical-grade silicon is mixed with slag. Different solubility of impurities in the molten silicon and in the slag or the existence of components in the slag that can form stable compounds with some of the impurities makes it possible to reduce the content of boron and phosphorous to below 0.5 parts per million weight (ppmw) and 1 ppmw, respectively [24,25].

After the slag treatment, the material is cast, grains solidify and grow until they meet other grains and form a grain boundary. This solidification process pushes contaminants to the grain boundary. In addition, impurities will diffuse to the grain boundary during cooling. In the leaching step, the silicon is ground to a powder, presumably divided at the grain boundaries, so that when the powder is subjected to acids (e.g. HF), the impurities can be etched off.

Directional solidification, as the name says, is a method to control the direction of the solidification, e.g., by using a heat sink to initiate crystallization. Some of the impurities have a higher solubility in liquid than in solid silicon, thus the concentration of these impurities will increase in the liquid silicon until the whole ingot is solidified, in the process known as segregation. If the solidification process is controlled to crystallize from the bottom to the top of the ingot, most of the impurities will be concentrated in the top part, which may be cut off in the post-treatment. In addition, it is well-known that the boron and phosphorus concentrations increase

with increasing ingot height. The distribution of each dopant or impurity element throughout the ingot height is described by the Scheil equation

$$C_{\mathrm{s}}(x) = k_{\mathrm{eff}} C_0 (1-x)^{(k_{\mathrm{eff}}-1)}, \tag{2.13}$$

where C_{s} is the impurity concentration in the solid as a function of the relative height, C_0 is the initial impurity concentration in the liquid and k_{eff} is the effective segregation coefficient. Scheil's equation assumes an ideal situation with zero diffusion in the solid, infinitely fast diffusion in the liquid and equilibrium at the presumably straight solid–liquid interface. The conventional segregation coefficient values are $k_{0,\mathrm{B}} = 0.8$ for boron and $k_{0,\mathrm{P}} = 0.35$ for phosphorus [26].

2.3.2 Compensation level

The primary characteristic difference between ESS™ and conventional polysilicon feedstock is the presence of phosphorus in addition to boron [27, 28]. These background phosphorous dopants are compensated for by the elevated acceptor (boron and/or gallium) levels, hence the name compensated silicon. 100 % ESS™ typically contains 0.6 ppmw phosphorus [24].

Compensated silicon is characterized by a *compensation level*, C_{l}, defined as

$$C_{\mathrm{l}} = \frac{N_{\mathrm{A}} + N_{\mathrm{D}}}{N_{\mathrm{A}} - N_{\mathrm{D}}}, \tag{2.14}$$

where N_{A} is the acceptor concentration and N_{D} is the donor concentration. In a non-compensated material, C_{l} is 1, and in a fully compensated material (N_{A}=N_{D}), C_{l} approaches infinity. In equlibrium, the majority carrier density in a p-type material is given by

$$p_0 = {N_{\mathrm{A}}}^{-} - {N_{\mathrm{D}}}^{+}, \tag{2.15}$$

where ${N_{\mathrm{A}}}^{-}$ and ${N_{\mathrm{D}}}^{+}$ are the concentrations of ionized acceptors and donors, respectively, and we have assumed $|N_{\mathrm{A}} - N_{\mathrm{D}}| \gg n_{\mathrm{i}}$. For simplicity, complete ionization, i.e., all acceptors and donors are ionized, is often assumed. Then ${N_{\mathrm{A}}}^{-}$=N_{A} and ${N_{\mathrm{D}}}^{+}$=N_{D}, and Equation (2.15) can be written as $p_0 = N_{\mathrm{A}} - N_{\mathrm{D}}$. The assumption of complete ionization does not always hold. In fact, incomplete ionization of the acceptors can occur when the acceptor doping level is $\sim 10^{17}$–10^{18} cm^{-3} [29]. Compensation doping, with the increased number of dopants, increases the number of potential scattering sites. Hence, the mobility is lower in compensated silicon.

2.4 Light- and Elevated Temperature-Induced Degradation in mc-Si

A slow degradation process in mc-Si solar cells under illumination and elevated temperatures has since its first observation [3] in 2012 been receiving significant research attention. This phenomenon, which was later named light and elevated temperature-induced degradation (LeTID) [4], can cause relative efficiency degradation of about 6–12 % in PERC solar cells [3–9]. Since its discovery, LeTID-behavior has also been observed in Czochralski (Cz) and float-zone (FZ) monocrystalline silicon material [30–32]. Extended exposure to the conditions that activate the degradation leads to a natural recovery of minority carrier lifetime which is termed "regeneration" [4, 9, 33]. At field conditions, the regeneration may take many years, in which the solar panels operate at reduced performance [4].

Current injection at elevated temperatures can also trigger this characteristic defect degradation, and thus a broader terminology of carrier-induced degradation (CID) is also commonly used in the literature. Relatively recently, several studies reported CID without optical or electrical carrier injection when investigating samples treated in the dark at elevated temperatures (known as dark anneal (DA) treatment) [7, 30, 34, 35]. In this work, the degradation is investigated by exposing HPMC-Si wafers to light at elevated temperatures, and thus the term LeTID will be used, and the literature review will focus on this approach and material.

2.4.1 What is LeTID?

As briefly described above, LeTID is a phenomenon causing degradation due to DA or high temperature combined with either illumination or current injection. This performance degradation has become a potential limiting factor for the development of *p*-type mc-Si high-efficiency PERC solar panels, despite the natural recovery in performance, due to the slow regeneration rates. Under similar testing conditions, LeTID and its regeneration have been observed on both cell and wafer level [3,4,36]. In addition, it is widely accepted that LeTID is caused by a bulk defect (or defects) [36–38].

2.4.2 Activation of the LeTID defect(s)

Understanding the wafer and cell processing conditions is important to determine whether and to what extent the LeTID defect will be activated [39].

The contact firing is known to be an activation step when the peak temperature is over approximately 700 °C, and the degradation extent is known to increase with higher peak temperature [5,36,40–42]. In addition, a hydrogen-rich dielectric layer must be present in this step [37]. Little to no degradation is observed when the wafer is fired without such dielectric passivation layer [43]. Sufficiently slow cooling rates from the peak firing temperature can suppress the degradation [44].

2.4.3 Injection dependence

Higher injection densities and increased temperature accelerate the degradation rate. Both the degradation rate and extent are also known to depend on the mode of operation (e.g., short or open circuit conditions) [4]. A directly proportional relationship between the degradation rate and illumination intensity has been observed [45, 46], and the degradation rate is shown to trend directly with the excess carrier density (Δn) in the wafer [47].

A difference in carrier injection level is hypothesized to be a suitable explanation for the difference in degradation behavior between PERC and other solar cell architectures (e.g., Al-BSF), since PERC tends to operate at higher injection levels [48]. It has been proposed that the LeTID defect formation may be limited by electron occupation of a particular precursor defect level [47]. The occupation probability of a defect determines its charge state in the wafer, and a change in charge state can trigger association or dissociation of metastable complexes [39]. Different solar cell architectures which operate at lower injection levles, as compared to PERC, may have a lower occupation probability for the LeTID precursor defect(s) under degradation due to the lower carrier injection level.

2.4.4 Root cause

Despite the intense research effort to study LeTID, the root cause is still unknown due to complexity of the defect. The fact that the carrier lifetime degrades over a prolonged period suggests an interaction between two or more components, which transform under degradation conditions [47]. Investigations have eliminated possibilities and generated a range of hypotheses for its constituents.

The light-induced degradation due to the activation of boron–oxygen (B–O) complexes as recombination sites was early discarded as the cause of degradation, as LeTID was detected in gallium (Ga)-doped wafers and wafers with varying interstitial oxygen concentration [3, 4]. Moreover, LeTID occurs on significantly longer timescales than those reported for B–O, also ruling out iron–boron (Fe–B) pairing effects which have higher dissociation rates [3, 4, 49, 50].

Metallic impurities are commonly suggested and evaluated based on solubility and diffusivity in silicon [36, 49–54]. Slightly less degradation towards the top of ingots has been observed [55–57]. Less degradation in wafers from the top of ingots could be caused by lower effective lifetimes and, therefore, slower degradation rates. It is also possible that the responsible defect may segregate during growth. Copper is one of the suggested impurities, which is present in mc-Si due to contamination in the material feedstock or the crucible in the casting process [58]. Yet, the timescales reported for copper-related LID appear to be too rapid [59–61].

Niewelt et al. discussed possible defect precursor species and ruled out several metallic impurities [62]. They created PL images at a fixed injection, so that the initial and degraded states could be evaluated at the same injection level. Thus, they avoided any misinterpretations in the spatially resolved investigations due to

the strong injection dependence of charge carrier lifetime in mc-Si. Thin regions of decreased degradation around grain boundaries (addressed to as denuded zones) were demonstrated in the state of minimum lifetime (i.e., maximum concentration of active defects) [62]. The total width of the denuded zones was found to be in the range of 200 to 400 µm [62]. Their result indicates that the defect, or an important precursor species, is internally gettered in the grain boundaries, which can occur either during crystallization, phosphorus diffusion or during the cooling after the final firing step. Thus, impurity species such as B, Ga, P, W, Ti, V, Oi, Zn and N were ruled out as they cannot form denuded zones of >100 µm width. These elements would need to form a complex with a more mobile species. Further, they found that Cr, Mn, Mo, Fe, Cu, Ni and Co cannot form denuded zones during the crystallization step. In agreement with the observation that LeTID is activated in the firing step, they found that the creation of the denuded zones is likely to occur during the firing step. The elements Cr, Mn, Mo and Fe were ruled out as they are too small to explain the width of the denuded zones. Possible candidates featuring diffusivities in a suitable range were found to be Cu, Ni and Co. Copper is, as mentioned above, an unlikely candidate. Nickel is also an unlikely candidate due to its quite high solubility. Cobalt has a suitable diffusivity, and it was highlighted as the most interesting candidate from the typical metal impurities for being involved in LeTID.

Hydrogen, by itself or in complexes, has been suggested as a potential candidate for causing LeTID [7, 30, 31, 33, 34, 36, 49, 63]. Some of these investigations have emphasized the properties of the passivating dielectric layers, in particular, the hydrogenated silicon nitride (SiN_x:H) film, which releases hydrogen into the Si bulk during firing [43, 51]. Introducing strategies to avoid or reduce the hydrogen in the bulk is not ideal to diminish LeTID in HPMC-Si since hydrogen has the important beneficial effect of passivating the grain boundary recombination of charge carriers [64, 65]. The phenomenon has also been connected to the hydrogen source itself by demonstrating LeTID through plasma hydrogenation [50]. Furthermore, an alternative defect model based on boron–hydrogen pairs has recently been proposed [66].

2.4.5 Mitigation strategies

Many strategies for LeTID mitigation have been suggested. These include: lower peak contact firing temperature, changes to the contact firing profile, design of high-temperature steps to control impurity distributions and accelerated formation and subsequent passivation of the defect [36, 40, 41, 44, 67–69]. The industry has adapted some of these strategies, and some manufacturers make modules that suppress LeTID or are claimed to be LeTID free [8]. Not all strategies can be beneficially applied to the solar cell process or finished solar cell devices at the industrial level. Understanding the root cause of LeTID is crucial to develop solutions that maximize device efficiency without the need for process- and/or material-specific optimization.

2.4.6 Kinetics

Comprehending the kinetics of the defect provides further insight into the fundamental nature of the degradation and may provide important clues regarding the root cause. Several approaches have been used to determine the time evolution of LeTID [35, 45, 47, 70, 71].

Kwapil et al. showed that the degradation rate constant depends linearly on the excess charge carrier density [47]. A single exponential function was used to extract the degradation and regeneration rates in that work.

Bredemeier et al. considered only the degradation part of the kinetics curve, when illuminating samples at 0.5 suns and temperatures 75–120 °C [45]. The investigated samples were non-compensated and had a resistivity of $1.66 \pm 0.03\,\Omega\,\mathrm{cm}$. They determined the presence of two defects, one slow and one fast. By applying Arrhenius analysis, they extracted the activation energies $E_{\mathrm{fast}} = 0.89 \pm 0.04\,\mathrm{eV}$, $E_{\mathrm{slow}} = 0.94 \pm 0.06\,\mathrm{eV}$ for the fast and slow defect, respectively [45].

Liu et al. extended the study on the kinetics of the defect to a large range of higher illumination intensities (14.6–74.5 $\mathrm{kW/m^2}$) using temperatures in the range 100–300 °C [46]. They investigated non-compensated wafers with a resistivity of $1.7\,\Omega\,\mathrm{cm}$. The degradation and regeneration activation energies were found to fall within the ranges of 0.62–0.78 eV and 0.67–0.78 eV, respectively.

Vargas et al. investigated the temperature dependence, as well as time evolution of the degradation and regeneration of samples under DA in the temperature range 138–300 °C [35]. The samples were non-compensated and had a resistivity of $1.70 \pm 0.02\,\Omega\,\mathrm{cm}$. They suggested that the degradation and regeneration happen simultaneously, and they proposed a model to support this suggestion. Activation energies were extracted using Arrhenius analysis and found to be $E_{\mathrm{deg}} = 1.08 \pm 0.05\,\mathrm{eV}$ and $E_{\mathrm{reg}} = 1.11 \pm 0.04\,\mathrm{eV}$ for the degradation and regeneration process, respectively [35]. The degradation activation energy is slightly higher than the ones reported by Bredemeier et al. [45], and the difference is attributed to the fact that illumination accelerates the degradation and regeneration processes. It is also mentioned that it is possible that the degradation mechanisms are different for DA and LeTID due to their stability [34]. Both the model suggested by Vargas et al. and the Arrhenius analysis will be described in Section 3.5.

Chen et al. investigated the impact of illumination and temperature in both n- and p-type silicon [70]. They obtained the degradation and regeneration rates by a similar model as the one proposed by Vargas et al. [35], but the model they used also takes into account a surface-related degradation (SRD) for the illuminated samples and a fast-forming defect during DA. Both the degradation and regeneration demonstrated similarities under DA and light soak (LS) (0.02 $\mathrm{kW/m^2}$) with $E_{\mathrm{deg,\,DA,\,slow}} = 0.76 \pm 0.02\,\mathrm{eV}$, $E_{\mathrm{deg,\,LS,\,slow}} = 0.70 \pm 0.05\,\mathrm{eV}$, $E_{\mathrm{reg,\,DA}} = 0.97 \pm 0.01\,\mathrm{eV}$ and $E_{\mathrm{reg,\,LS}} = 0.83 \pm 0.15\,\mathrm{eV}$ [70]. The activation energies for the DA treatment are lower than those reported by Vargas et al. [35], which was hypothesized to be due to the different materials used (mc-Si vs. Cz-Si), particularly

if hydrogen is involved in LeTID degradation and regeneration [70]. Furthermore, the fast degradation was determined to be $E_{\text{deg, DA, fast}} = 0.30 \pm 0.10\,\text{eV}$, and the SRD observed under illumination is determined to have $E_{\text{SRD}} = 0.38 \pm 0.10\,\text{eV}$. The exact meaning of the SRD activation energy remains unclear [70].

Chapter 3

Experimental Details

This chapter is divided into five parts. First, the details of the sample preparation are given, followed by a short description of the most important lifetime characterization techniques used in this study. Then the meaning of the unit sun in the context of this work is explained, and the different treatment groups for LeTID investigations are presented. Subsequently, the representation of lifetime values is described. Finally, a presentation of the model used to calculate degradation and regeneration rates and the procedure for extracting activation energies is given. All the described measurements were performed in the solar cell laboratory at IFE.

3.1 Sample Preparation

3.1.1 Ingot material

In this work, the investigated wafers are from a corner brick of a commercially cast HPMC compensated silicon ingot. As noted in Section 2.3.2, this type of silicon contains both donors and acceptors added in the feedstock. For this particular ingot, boron–gallium co-doping is used, which means that the remaining phosphorous donor concentration after the proprietary purification process used by REC Solar Norway is compensated by adding both boron and gallium as the acceptors. The aim of the co-doping is to create a more uniform resistivity profile throughout the height of the ingot.

The doping levels and their variation with relative ingot height were estimated using the Scheil equation (2.13) with initial doping levels provided by the manufacturer. Figure 3.1.1 shows a plot of the estimated doping levels, compensation level and resistivity profile.

The manufacturer cut the brick into square, $156 \times 156\,\mathrm{mm}^2$ wafers which were measured to be $191 \pm 2\,\mu\mathrm{m}$ thick.

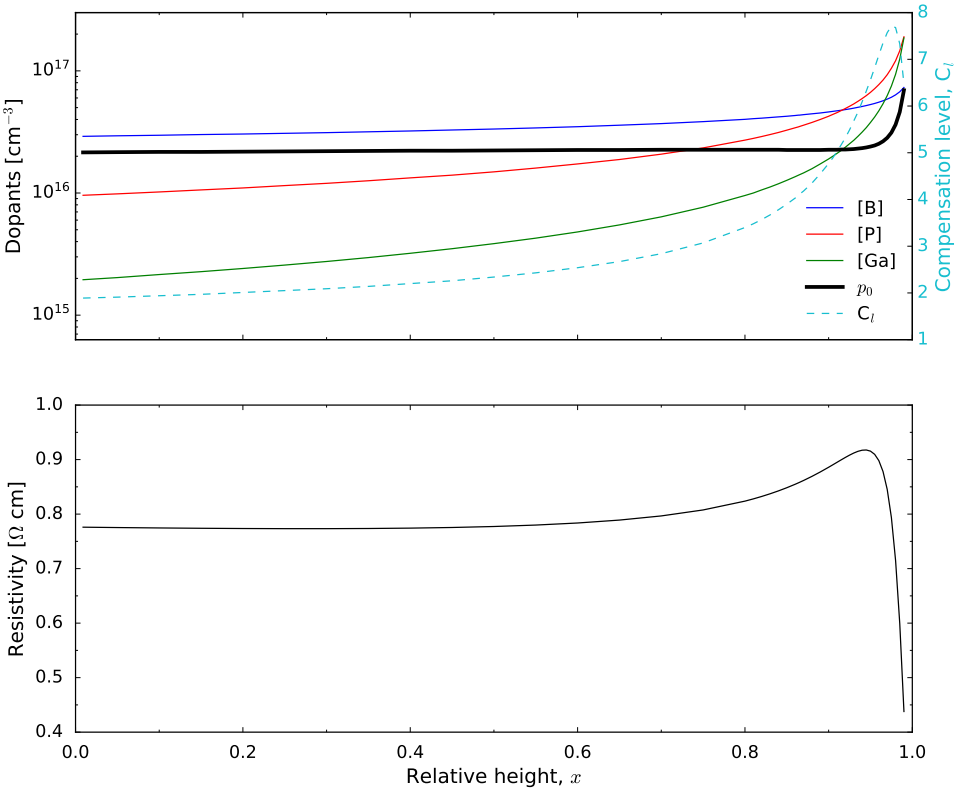

Figure 3.1.1: Top: Doping levels estimated from Scheil equation (2.13) for B, P and Ga throughout the height in the ingot. **Bottom**: Resistivity profile. A bottom slab of about 10 % and a top slab of about 5 % are typically removed before wafering.

3.1.2 Wafer processing

Twenty-five wafers were selected from sister positions of $\sim$ 30–40 % height in the ingot with measured resistivity $0.7 \pm 0.03\,\Omega\,\mathrm{cm}$. Note the offset between the measured resistivity and the calculated resistivity profile (Figure 3.1.1). A comparable material quality, as well as very similar grain and defect structure, can be ensured by using sister wafers.

To show the improvement in bulk lifetimes after different stages in the simulated solar cell processing, the wafers were divided into three groups according to Figure 3.1.2. Wafers of **Group I**, called ungettered (alternatively as-cut (AC)), have not been subjected to any high-temperature processing steps after the casting process. All wafers have, however, been saw-damage etched in a HNA-solution ($HF:HNO_3:CH_3COOH$) in order to clean the wafers and remove any damages on the surface. Approximately 9 µm is etched off in this step, which was repeated twice for the **Group I** wafers to obtain comparable optical properties and thickness to the wafers in the two other groups.

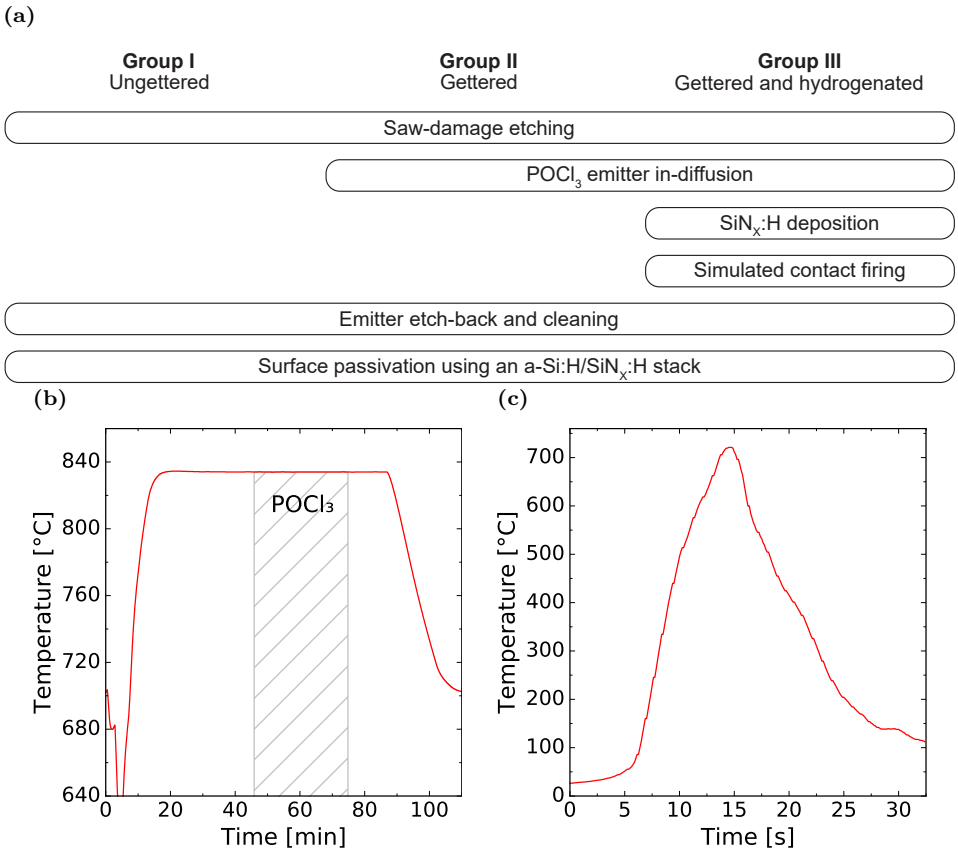

Figure 3.1.2: **(a)**: Wafer preparation prior to lifetime measurements. The wafers were divided into three groups to show the improvement in bulk lifetimes after different stages in the simulated solar cell process. All wafers were etched together in order to obtain comparable surface properties. **(b)** and **(c)**: Temperature profiles for the phosphorus in-diffusion and the simulated contact firing, respectively. The temperature profiles were measured by Rune Søndenå using a thermocouple inside the tube furnace during the emitter in-diffusion and by placing a thermocouple on a wafer during the firing process.

Group II and **Group III** wafers, called phosphorus diffusion gettered (PDG) and phosphorus diffusion gettered and hydrogenated (PDGH), respectively, underwent a dual side phosphorus diffusion using phosphoryl chloride ($POCl_3$) as the dopant source. This step creates the n^+-emitters with a sheet resistance, R_{sheet}, of $65 \pm 2\,\Omega/\square$, measured on dummy wafers diffused in parallel using a four-point probe. The reported sheet resistance is measured from a $100 \times 100\,\text{mm}^2$ region in the centre of the wafer, where edge effects do not interfere with the measurements. A short treatment in HF is used to remove any phosphosilicate glass left on the surface after diffusion. The entire gettering step leads to removal of fast diffusing metal impurities [72].

Subsequently, an anti-reflection coating (ARC) of a hydrogen-rich SiN_x was deposited on wafers of **Group III** through direct plasma-enhanced chemical vapor deposition (PECVD) in a lab-scale parallel plate reactor (Plasmalab 133 from Oxford Instruments) using ammonia and a silane/nitrogen mixture as process gases. Immediately before loading the wafers into the vacuum system, the wafers were immersed in HF to remove the native oxide layer. To introduce hydrogen into the silicon bulk from the SiN_x:H films, wafers underwent simulated contact firing (temperature profile in Figure 3.1.2c) using a RTC LA-309 infrared metallizaton belt furnace at a belt speed of 5.2 m/ min. As hydrogen diffuses into the bulk of the wafers, structural defects such as grain boundaries are expected to become partly or completely passivated.

The ARC and the n^+-layer were wet-chemically removed in a new HNA-solution (emitter etch-back). Lastly, wafers of all groups were cleaned in a Piranha solution (H_2O_2:H_2SO_4) and surface-passivated with an a-Si:H/SiN_x:H stack using PECVD. Typical thickness of the a-Si and SiN_x:H are 43 nm and 80 nm, respectively. This resulted in $173 \pm 2\,\mu m$ thick wafers ready for lifetime measurements. Excellent surface passivation is obtained, so we can consider the effective lifetime to reflect the actual lifetime in the bulk material.

Once processed, nine $50 \times 50\,mm^2$ lifetime samples were laser carved from each PDGH wafer and split into different treatment groups as described in Section 3.3.2. The samples were immediately stored in the dark at room temperature to avoid any lifetime changes due to ambient light in the laboratory.

3.1.2.1 Sample processing impact on lifetime

Sample processing mitigates the effect of defects and impurities present after crystallization, and it thus affects the carrier lifetime. Calibrated PL lifetime maps of as-cut, PDG and PDGH commercially cast HPMC wafers illustrate the effect of processing in Figure 3.1.3a. The as-cut wafer does not undergo any sample processing for lifetime improvement and is included as a reference to quantify the improvement of impurity gettering and defect passivation. It can be seen that each processing step increases the overall lifetime in the wafer. A close-up (Figure 3.1.3b) has been included to illustrate the effect of sample processing on lifetime more evidently. (The zoomed-in area is indicated by the dashed square in Figure 3.1.3a.)

As can be seen, the lifetime value over the wafer is higher for the PDG wafer compared to the as-cut. This is especially evident in the close-up, showing two effects: (1) The lifetime decreases in the grain boundary region, (2) while the lifetime increases remarkably inside grains.

Impurities like oxygen and metallic fast-diffusers such as Fe, Ni, Cr and Cu can be found in mc-Si. These impurities have different solubility and diffusion properties. External gettering can efficiently remove fast-diffusing impurities (as the ones mentioned above). The effect can be described as follows: During the PDG processing step, oxygen and phosphorous impurities, as well as complexes of these,

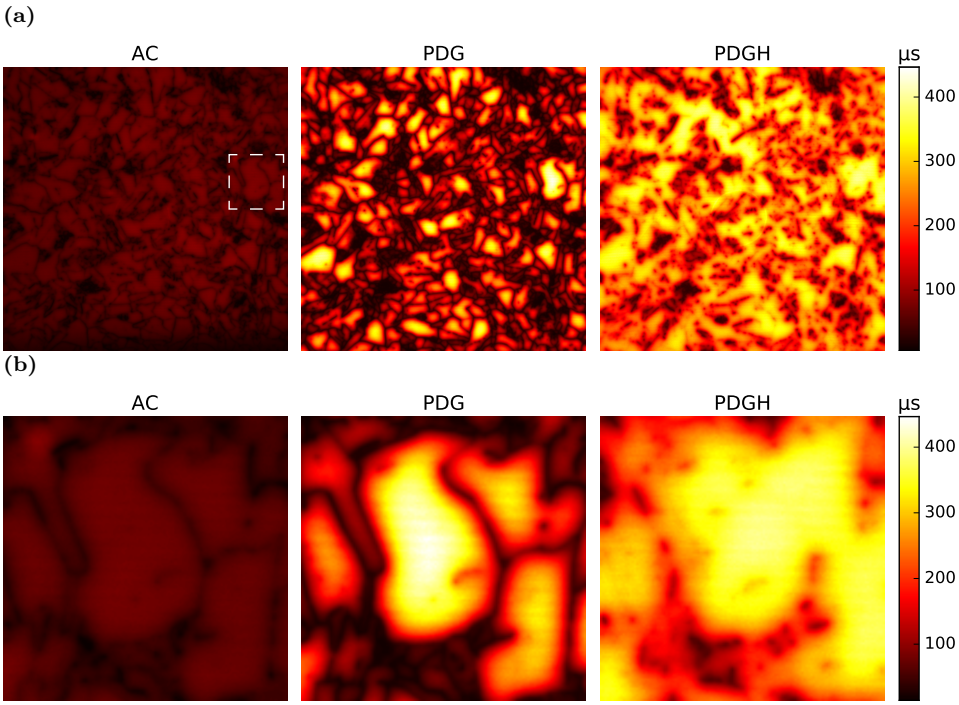

Figure 3.1.3: **(a)**: Calibrated PL lifetime maps for three sister wafers from about 40 % of the ingot height. The lifetime values were measured at room temperature and extracted at $\Delta n \approx 0.1 \cdot p_0$, corresponding to an injection level of about $2.2 \cdot 10^{15}\,\mathrm{cm}^{-3}$. The dashed square of the as-cut map defines the zoomed-in area in **(b)** that shows a close-up of the wafers, which makes the effect of the processing steps easier to see.

are delivered to the wafer from the applied $POCl_3$. These serve as nucleation sites. The impurity diffusion to grain boundaries and dislocation clusters (internal gettering) may cause intra-grain lifetime enhancement. This may describe, or at least partly describe, the high recombination activity (low lifetimes) observed at grain boundaries. High-temperature diffusion (∼900 °C), as performed in the PDG step, can lead to both impurity diffusion and structural defect annealing [73]. The effect of gettering in dislocation-rich areas is less efficient [74].

Turning now to look at the PDGH wafer, it can clearly be seen that the overall lifetime in the entire wafer has increased compared to the PDG wafer. Note also that the grain boundaries have changed from sharp and well-defined low-lifetime areas to blurred higher-lifetime areas. Hydrogen can passivate defects, impurities and segregated impurities on extended defects [75]. Grain boundaries feature an increased number of impurities and more dislocations, which can explain why we observe and expect hydrogenation to be more beneficial at grain boundaries than in grains.

3.2 Carrier Lifetime Measurements

Carrier lifetime can be determined using several different methods, most of which depend on measurements of the excess carrier density. Excess carrier density can be contactless measured by, e.g., measuring the current generated in an inductively coupled coil or the free carrier absorption of infrared light. The coil-based QSSPC and the high spatial resolution imaging of the band-to-band photoluminescence (PL) are utilized in this work and described in the following.

3.2.1 Quasi-steady state photoconductance measurements

The QSSPC method, as first suggested by Sinton and Cuevas [76, 77], is used mainly for lifetime measurements, but it can also be used for resistivity and saturation current measurements. This technique can briefly be described as follows: The wafer, which is to be measured, is illuminated by light from a flash lamp with an adjustable decay time constant. An inductively coupled coil measures the conductivity of the sample under illumination, which in turn can be used to calculate the excess carrier density. Thus, the injection level can be measured in a fast and elegant way. By selecting either a long or short time constant of the flash decay, the user chooses to conduct the measurements in the *quasi-steady state* or the *transient* case, respectively. In general, however, it is possible to use a generalized analysis applicable to measurements of longer lifetimes, in the same range or larger than the decay constant of the flash. This *generalized case*, proposed by Nagel et al. [78], is used for all measurements presented in this study. Figure 3.2.1 shows a schematic diagram of the Sinton Instruments WCT-120TS QSSPC setup used in this work.

The first step for the general analysis is the continuity equation for the excess carrier density,

$$\frac{\partial \Delta n}{\partial t} = G(t) - U(t) + \frac{1}{q}\nabla \boldsymbol{J}. \tag{3.1}$$

To ensure a homogeneous generation all over the wafer, the Sinton QSSPC is set up with a Xenon flash with a longpass filter. This means that the gradient of the current density, $\nabla \boldsymbol{J}$, can be estimated to zero with only a small error. Inserting the relationship $U = \Delta n/\tau_{\text{eff}}$ from Equation (2.1) and solving for τ_{eff}, Equation 3.1 can be written as

$$\tau_{\text{eff}} = \frac{\Delta n(t)}{G(t) - \frac{\partial \Delta n(t)}{\partial t}}. \tag{3.2}$$

Measurements of τ_{eff} in the generalized analysis are thus dependent on both the injection level and the generation rate in the wafer as a function of time. The injec-

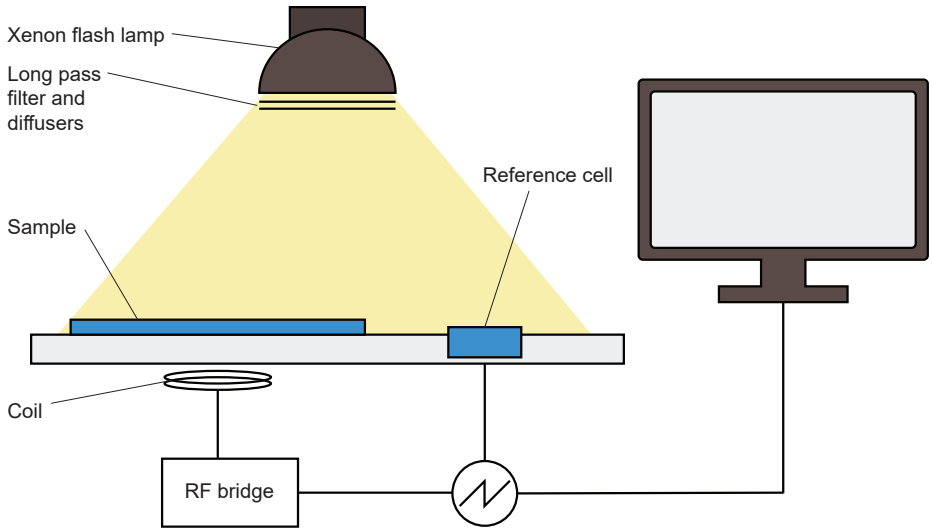

Figure 3.2.1: Schematic diagram of the Sinton WCT-120TS instrument used for the QSSPC measurements. The flash lamp illuminates the sample which generates electron–hole pairs. The photoconductance and the flash lamp intensity are simultaneously recorded with a radio frequency bridge and a solar reference cell, respectively.

tion level is determined from the recorded changes in the excess photoconductance $\Delta\sigma(t)$ of the sample, measured in the coil as

$$\Delta n = \frac{\Delta\sigma(t)}{q(\mu_\mathrm{n} + \mu_\mathrm{p})W}, \tag{3.3}$$

where μ_n and μ_p are the electron and hole mobility and W is the wafer thickness.

The generation rate is measured as

$$G(t) = OC \cdot \frac{I_\mathrm{ref}(t)}{qW_\mathrm{ref}}, \tag{3.4}$$

where I_ref is the generated photocurrent measured by the solar reference cell, and OC is the optical constant determined by the optical properties of the sample as compared to the reference diode. Values for OC can be found for a range of different surface coatings in the Sinton WCT-120TS manual. Ultimately, Equation (3.2) can be used to calculate the effective lifetime at each injection level.

In this work, the Sinton WCT-120TS instrument was used mainly for resistivity measurements. Prior to the QSSPC measurements, a BT Imaging LS-R1 PL-I instrument (as described in Section 3.2.2) was used to take PL-images of the wafers. These images were used to determine the optimal position to place the wafers on the measuring coil in the QSSPC setup.

The QSSPC coil has a diameter of about 16.5 mm, and it can thus only measure a small section of the wafer in one measurement. An arbitrary measurement position is not necessarily representative for the whole wafer. If possible, the measurements were conducted on large, high-lifetime grains. This choice was made because it gave the most consistent results in the QSSPC measurements. One must also take into account that the dislocation clusters usually are smaller and more dispersed in the lower part of the ingot, and they become larger and more localized toward the top [79].

3.2.2 Photoluminescence-imaging measurements

Photoluminescence-imaging (PL-I) is, with its high resolution and short measurement time, a versatile technique for the characterization of silicon samples across almost the entire PV value chain [80–82]. The method is contactless and non-destructive. In brief, the setup works as follows: Light from a diode laser is directed onto a sample which is optically excited to emit luminescence. The resulting variation in PL emission is detected by a charge-coupled device (CCD) camera. Ultimately, 2D maps of the effective lifetime over a wafer is acquired. A schematic diagram of the LIS-R1 instrument from BTImaging used in this work is shown in Figure 3.2.2.

The band-to-band emission rate, Φ_{PL}, of an illuminated silicon sample equals the rate of radiative recombination from Equation (2.7),

$$\Phi_{\mathrm{PL}} = B_{\mathrm{rad}}(np - {n_{\mathrm{i}}}^2). \tag{3.5}$$

For moderately doped p-type material, where $p = N_{\mathrm{A}} + \Delta n$, $n = \Delta n$ and n_{i} may be neglected, the measured intensity, I_{PL}, can then be written as

$$I_{\mathrm{PL}} = C_{\mathrm{cal}} B_{\mathrm{rad}}(N_{\mathrm{A}} + \Delta n)\Delta n, \tag{3.6}$$

where C_{cal} is a sample and instrument specific calibration constant describing the fraction of the emitted light which is detected by the camera. This constant can be determined by an independent lifetime measurement by a stand-alone QSSPC instrument (as described in Section 3.2.1) or by the built-in QSSPC in the PL-I setup, and the constant is used to calculate the effective lifetime at each point in the PL image. Rearranging Equation 3.6 to calculate C_{cal} yields

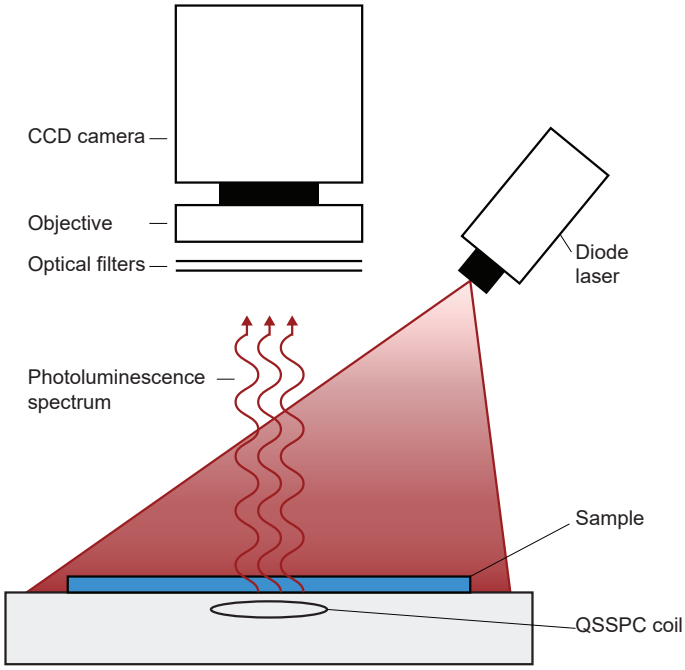

Figure 3.2.2: Schematic diagram of the BT Imaging LS-R1 instrument used for the PL-I measurements. The diode laser injects carriers homogeneously over the full sample and the generated PL signal from the thermalization of carriers is detected by a CCD camera.

$$C_{\mathrm{cal}} = \frac{I_{\mathrm{PL,cal}}}{B_{\mathrm{rad}}(N_{\mathrm{A}}\Delta n_{\mathrm{cal}} + \Delta n_{\mathrm{cal}}^2)}, \tag{3.7}$$

where I_{PL} is the PL intensity in the region above the coil.

For low-injection conditions, $p = N_{\mathrm{A}}$, the injection level Δn is simply proportional to the measured intensity,

$$\Delta n(x, y) = \left(\frac{1}{C_{\mathrm{cal}} B_{\mathrm{rad}} N_{\mathrm{A}}}\right) \cdot I_{\mathrm{PL}}(x, y). \tag{3.8}$$

PL images are acquired at steady state conditions. This means that the effective lifetime can be obtained from the injection level as

$$\tau_{\mathrm{eff}}(x, y) = \frac{\Delta n(x, y)}{G} = \frac{\Delta n(x, y)}{(1 - R_f)\Phi_{\mathrm{ph}}/W}, \tag{3.9}$$

where R_f is the front reflectance, Φ_{ph} is the photon flux from the excitation and W is the thickness of the wafer.

Uncalibrated PL intensity images were recorded for all wafers, using this band-to-band photoluminescence imaging technique during uniform illumination with a 808 nm laser, on the LIS-R1 instrument [81–84]. The PL instrument takes doping type, resistivity, sample thickness and weight and reflectivity data as input. Reflectivity was measured using an Ocean optics stage-RTL-T. The average reflectance can be seen in Figure 3.2.3 and was found to be 10 % at 808 nm. An in-house MATLAB-script was used to calculate the calibration constant.

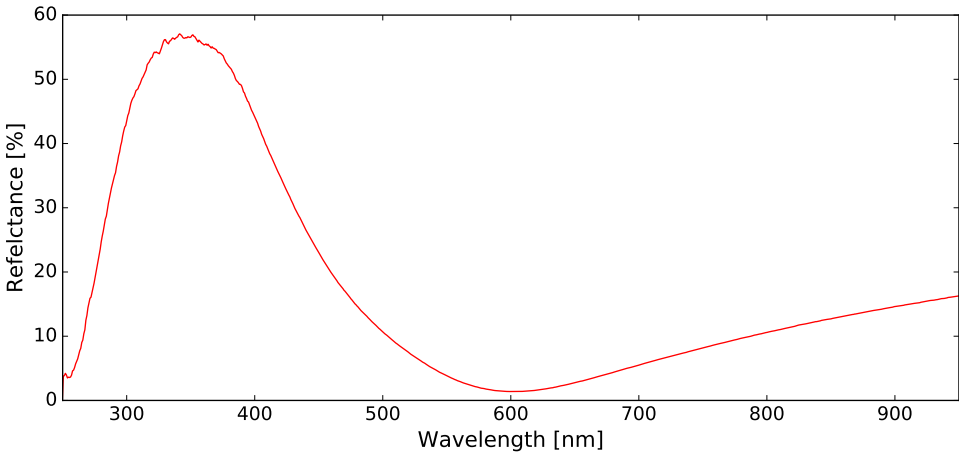

Figure 3.2.3: Average reflectance of the lifetime samples. The average reflectance at 808 nm was found to be 10 %.

3.3 Light Soaking at Elevated Temperature

In this work, LeTID is investigated by exposing the lifetime samples to light at elevated temperatures. A LED-based illumination source is used, thus the need for calibration with respect to the entities of the sun arises. The calibration procedure used in this work is explained first in this section, followed by a presentation of the different light soak processes used. For simplicity, the term "treatment" will be used in the following to denote light soaking at elevated temperatures.

3.3.1 Meaning of sun equivalents

Virtually no laboratory investigations of light-induced degradation (LID) utilize the sun directly, but rather use different light sources, e.g., halogen- and LED-based illumination. Due to fundamental differences in the spectra from these light sources, it is convenient to quantify and match the entities of the sun to solar simulators and light soakers. This calibration procedure is not as straightforward as it might seem.

The rather undefined unit of "suns" or "sun equivalents" are often used to report the light intensity in LID studies. These expressions most probably originate from standard test conditions (STC) defined in IEC 60904 [85]. One sun is then defined from the suns reference spectrum ASTM G173 (Figure 3.3.1), known as reference spectrum AM1.5. Approximating the sun as a black body of ∼5800 K yields a standardized total power density, p_{G173}, of 100 mWcm^{-2} by

$$p_x = \int_0^\infty \Phi_x(\lambda) \cdot \frac{hc}{\lambda} d\lambda. \tag{3.10}$$

The p_{G173} can be linked to a usable photon flux $\Phi_{\mathrm{G173}}(\lambda) = p_{\mathrm{G173}}/(hc/\lambda) = 2.7 \cdot 10^{17}\,\mathrm{cm}^{-2}\mathrm{s}^{-1}$ (where hc/λ is the photon energy) for the crystalline silicon cell conversion wavelength range 320–1100 nm according to the definition

$$\phi_x = \int_{320\ \mathrm{nm}}^{1100\ \mathrm{nm}} \Phi_x(\lambda) d\lambda. \tag{3.11}$$

However, it has been shown that for deviating spectra, power density and photon flux scale differently and are dependent on the interpretation of the unit "sun" [86]. How the usable photon flux is defined is therefore a question of definition. The generation density, g, is the most relevant entity for most LID experiments and is defined as all photons not lost by reflection, $R(\lambda)$, transmisson, $T(\lambda)$, or parasitic absorption, $A(\lambda)$, according to

$$g = \int_{320\ \mathrm{nm}}^{1100\ \mathrm{nm}} \Phi(\lambda) \cdot (1 - R(\lambda) - T(\lambda) - A(\lambda)) d\lambda. \tag{3.12}$$

As the generation is hardly determinable, three other approaches are commonly used: One is to match the total power density $p_x = 100\,\mathrm{mWcm}^{-2}$, another is to match the photon flux $\Phi_x = 2.7 \cdot 10^{17}\,\mathrm{cm}^{-2}\mathrm{s}^{-1}$ and some authors refer to a comparable short circuit current density, j_{sc}, equivalent. Clearly stating the chosen calibration procedure is crucial to ensure that, e.g., experimental results on reaction rates – which may depend on injection level and thus generation – are reproducible.

This study utilizes a LED-based light-soaking system from Wavelabs with an integrated hotplate with capacity for up to 450 °C in device temperatures. The actual spectral irradiance had never previously been measured in the solar cell laboratory at IFE. To do so, a PSR-1100F portable spectroradiometer from Spectral Evolution was used for direct energy measurements. By placing the sensor inside the light soaker at the same height as the hotplate (on which the wafer is placed), the best possible detection was obtained. Figure 3.3.1 shows some of these measurements as well as the 1-sun AM1.5 reference spectrum.

The gathered data was used to calculate measured irradiance at a range of setpoints. Due to the spectral mismatch between the virtually monochromatic spectrum of light soaker LED-lamps and the broad blackbody sun AM1.5 spectrum, the "suns

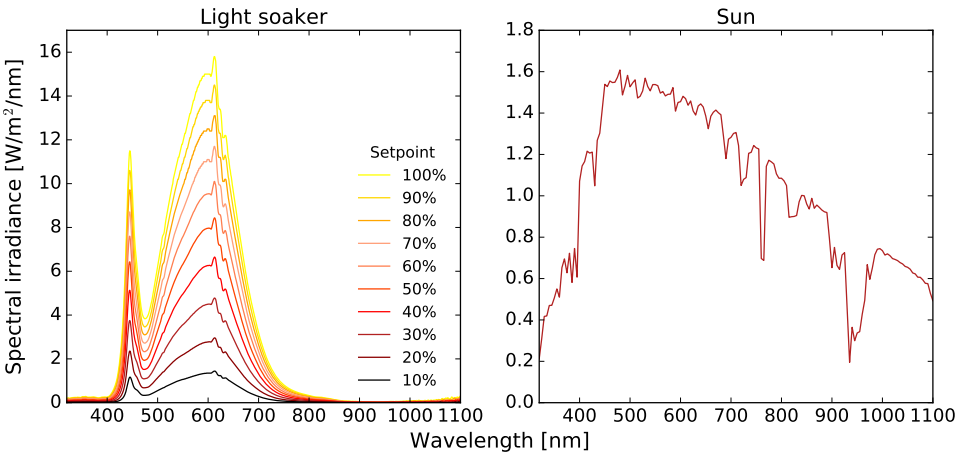

Figure 3.3.1: Left: Measured spectral irradiance of the light soaker used in this work and **right:** sun AM1.5 reference spectrum.

equivalent" illumination is approximated by comparing the calculated photon flux of the light soaker to the AM1.5 spectrum as plotted in Figure 3.3.2. Note that for LED-lamps virtually every photon contributes to the generation of excess charge carriers. *The unit "suns" in this thesis refers to sun-equivalents with respect to* Φ_{G173}.

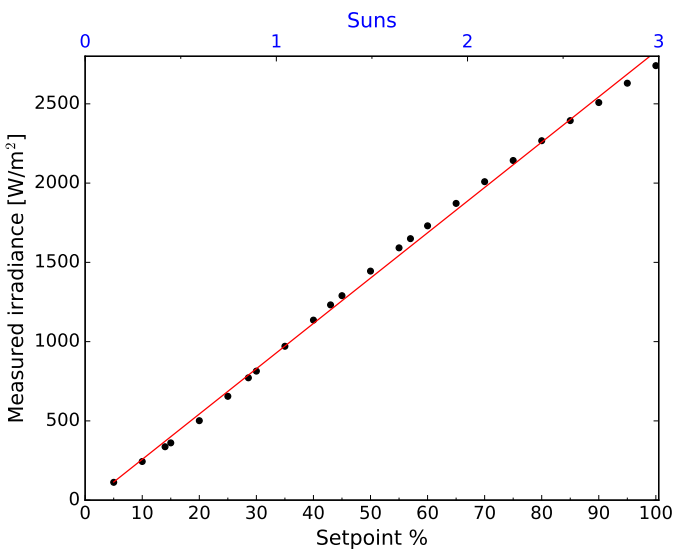

Figure 3.3.2: Measured irradiance as function of setpoint on the light soaker and corresponding suns generation equivalents with respect to the usable photon flux, Φ_{G173}. The red line is a linear fit.

3.3.2 Treatment groups

The lifetime samples of **Group III** (the gettered and hydrogenated samples) were divided into three treatment groups according to Figure 3.3.3. All wafer temperatures were measured by an infrared temperature sensor. In the following, the terms "sister" and "neighbor" wafers will be used to denote lifetime samples laser carved from the same position but different height in the ingot (subsequent wafers) and from different positions in the same wafer, respectively.

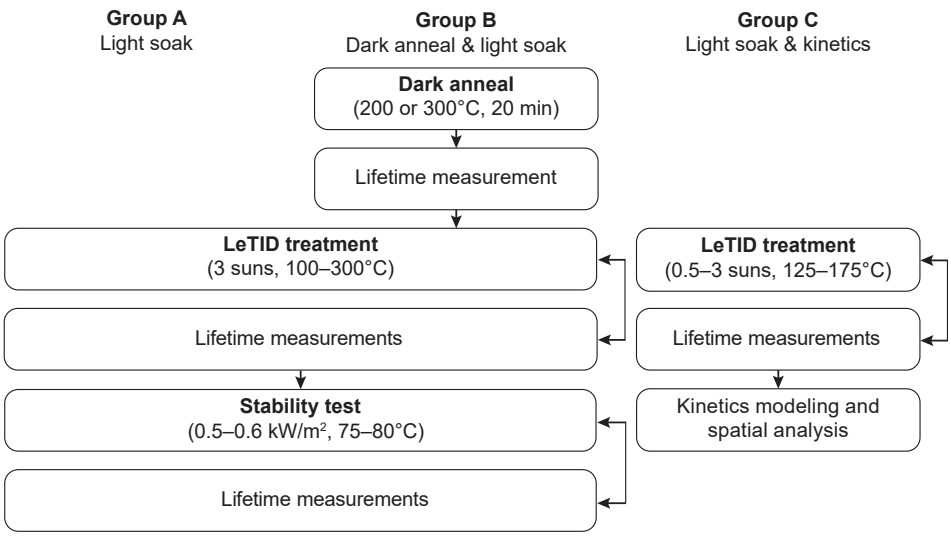

Figure 3.3.3: Treatment groups for LeTID investigations.

Accelerated degradation and regeneration of LeTID was tested on seven sister wafers of **Group A** illuminated at 3 suns and with annealing temperatures ranging from 100 to 300 °C. Some of these wafers were selected for a stability test, where the regenerated samples were placed on a hotplate and subjected to light soaking at 75–80 °C under a white LED light source with incident irradiance of 0.5–0.6 kW/m^2. Note that the reported temperature and intensity interval for the stability test are due to an inhomogeneous hotplate and lamp. One sister wafer was kept as a non-treated reference sample.

To investigate the impact of DA prior to accelerated degradation and regeneration, two sets of sister wafers were chosen for **Group B**. Both sets were dark annealed for 20 min – at 200 °C and 300 °C, respectively – prior to a LeTID-treatment at 3 suns with annealing temperatures 150–300 °C in 25 °C intervals. To avoid confusion, the samples with pre-DA at 200 °C will be referred to as **Group B**$_{200\,°C}$ and the samples with pre-DA at 300 °C will be referred to as **Group B**$_{300\,°C}$. One wafer from each set was used to monitor the lifetime evolution during the DA-step. The wafers regenerated at 150, 200 and 300 °C from each set were chosen for a stability

test, with the same test conditions as for wafers of **Group A**.

Group C: Sixteen treatment conditions were chosen to investigate the temperature and illumination dependencies of the reaction rates. Only 13 sister wafers were available, so these had to be supplemented by three neighbor samples which were chosen to have the closest initial lifetime possible. The samples were illuminated at 0.5, 1, 2 and 3 suns, respectively, with temperatures in the range 125–175 °C.

The samples were continuously illuminated, only interrupted by periodical lifetime measurements, once the experiment started to exclude possible effects from dark storage. Further, all samples were manually removed from the light-soaking system after each illumination allowing for air cooling to room temperature. Effective lifetime was monitored periodically by incremental PL and QSSPC measurements using the LIS-R1 instrument described in Section 3.2.2. Lifetimes were extracted at an injection level of $\Delta n \approx 0.1 \cdot p_0$, corresponding to an injection level of about $2.2 \cdot 10^{15}\,\mathrm{cm}^{-3}$.

3.4 Representation of Lifetime Values

The evolution in carrier lifetime due to LeTID is in this work presented using the normalized effective lifetime defined as

$$\tau_{\mathrm{norm}} = \frac{\tau(t)}{\tau_0}, \tag{3.13}$$

where $\tau(t)$ denotes the effective minority carrier lifetime measured during LeTID testing and τ_0 is the lifetime measured after processing.

For simplicity, a single spatially averaged lifetime value can be extracted from the lifetime images that contain a lifetime value in each pixel. Choosing an averaging procedure to represent inhomogeneous wafers is a nontrivial task. The generalized average for a set of measured lifetimes can be defined as

$$\langle \tau \rangle_p = \left[\frac{1}{N} \sum_{i=1}^{N} \tau_i^p \right]^{\frac{1}{p}}, \tag{3.14}$$

where p defines the type of average obtained. Two approaches are commonly used: (1) Simply forming the arithmetic mean ($p = 1$) of measured lifetimes or (2) assuming that the recombination strength is the additive parameter and may thus be averaged by an arithmetic mean [87]. Since the recombination rate is $R = 1/\tau$, this is equivalent to the harmonic average of the measured lifetime values ($p = -1$). This averaging procedure is better for taking into account lifetime-limiting low-lifetime regions.

Several studies have compared these averaging procedures with respect to assessment of material quality. Sio et al. found that the harmonic average gives a closer

approximation to the actual cell efficiency than the arithmetic average, but still overestimates the cell efficiency particularly on wafers with high density of crystal defects [88]. Isenberg et al. found that the arithmetic average overrate the high-lifetime regions, while the harmonic average "over-corrects" this shortcoming of the arithmetic average and thus overrate the low-lifetime regions, and the study thus proposed a weighted mean procedure for finding a middle value [87]. Still, the harmonic average was found to yield more reasonable results than the arithmetic average.

In this study, arithmetic average was chosen to minimize the impact of any consequential scratches (may cause low-lifetime regions) in the passivation layer by manually removing the wafers from the light soaking device.

To analyse the defect, the normalized defect density (NDD) defined as

$$\mathrm{NDD}(t) = \frac{1}{\tau(t)} - \frac{1}{\tau_0}, \tag{3.15}$$

is used. This approach assumes that the amount of LeTID that may pre-form during the simulated contact firing step is negligible compared to the quantity formed under LS experiments [30]. It is also important to note: (1) This definition assumes that only a single-defect species changes in between lifetime measurements, (2) NDD in units of [s^{-1}] should not be confused with the actual defect density in units of [cm^{-3}] and (3) NDD is injection- and temperature-dependent, thus, it should be clearly stated at which injection and temperature it was determined to allow for comparison with other investigations [89].

When quantifying the changes in bulk minority charge carrier lifetime via the lifetime-equivalent NDD, one should be aware of possible pitfalls [89]. The NDD should be treated with caution if the assumption within the derivation of NDD are not met, especially if not just one recombination channel changes but two or more. Another common pitfall encountered particularly in laterally inhomogeneous multicrystalline materials is to compare the NDD of regions or grains with different lifetime [89]. The PL technique, as used in this work, determines an effective lifetime not at a certain injection level, but at a certain constant generation according to

$$G \cdot \tau_{\mathrm{eff}} = \Delta n \propto \Phi_{\mathrm{PL}}. \tag{3.16}$$

Neglecting the injection dependency, or the lack of truly injection dependent τ_{eff} data, could lead to misinterpretations when comparing the impact of LeTID in different grains. Heinz et al. proposed an approach to implement a countermeasure to avoid this possible misinterpretation [90]. Note that this is beyond the scope of this work.

3.5 Degradation and Regeneration Rates Calculation and Activation Energies

3.5.1 Determination of reaction rates

A model proposed by Vargas et al. [35] was used to determine the degradation and regeneration rates. The model is described by the following expression:

$$\mathrm{NDD}(t) = \mathrm{NDD}_{\mathrm{max}}\{[1 - \exp(-r_{\mathrm{deg}}t)] - (1 + A)[1 - \exp(-r_{\mathrm{reg}}t)]\}, \tag{3.17}$$

where $\mathrm{NDD}_{\mathrm{max}}$ is the maximum possible NDD, A is a factor to account for any lifetime improvement obtained during the process, and r_{deg} and r_{reg} are the degradation and regeneration rates, respectively.

This model assumes: (i) one defect, (ii) degradation and regeneration occurs simultaneously (since the process conditions do not change during the entire time duration), (iii) the maximum amount of defects is related with only one parameter (NDDmax) and (iv) the additional factor A is used to describe any lifetime improvement obtained by the process [35]. This model is a semi-empirical approach, limited to cases where the rates can be considered constant.

The Python algorithm `curve_fit` from the module `scipy.optimize` – which uses bound-constrained non-linear least squares – was used to fit the experimental data to this model [91].

3.5.2 Activation energy extraction

The Arrhenius equation, which gives the dependence of the degradation and regeneration rates on the absolute temperature, is defined as

$$r_{\mathrm{deg/reg}} = C \cdot \exp\left[-\frac{E_{\mathrm{deg/reg}}}{kT}\right], \tag{3.18}$$

where C is a constant, k is the Boltzmann constant, T is the temperature (in Kelvin) and $E_{\mathrm{deg/reg}}$ are the degradation and regeneration activation energies, respectively. Activation energies can be calculated by considering the linearized Arrhenius equation

$$\ln r_{\mathrm{deg/reg}} = -\frac{E_{\mathrm{deg/reg}}}{k}\left(\frac{1}{T}\right) + \ln C. \tag{3.19}$$

Thus, a plot of $\mathrm{r}_{\mathrm{deg/reg}}$ as a function of T^{-1} gives a straight line, whose gradient and intercept can be used to determine $E_{\mathrm{deg/reg}}$ and C.

3.5.3 A possible pitfall of least squares fit in physics applications

Caution is required when using least squares fitting in physics applications. Here, the lifetime measurement uncertainty restricts sensitivity in the NDD. A relative uncertainty of 1–8 % is considered a good estimation for the uncertainty in lifetime measurements [89]. Further, we consider a 2 °C uncertainty in the measured temperatures. Not only should one take these measurement uncertainties into account, but one should also consider the uncertainties associated with the fit algorithm(s).

One approach is to simply ignore the presence of errors and use the ordinary least squaress method. This method is consistent when all experimental variables have the same finite variance. However, most experimental data have errors that vary from point to point. Some might just include the errors as error bars in the graph. When error bars are only included in the plot, it is often obvious that they should have been used in the calibration. Ignoring errors that vary from point to point gives no better fit than an estimation by eye.

Thus, any least squares analysis should identify if the fit should involve weights to include the effect of these errors. This need for a weighted least squares fit can arise in several ways, including: (1) when the data are a combination of two or more sets with different error characteristics, (2) when the data are transformed by some function of the independent variable before the fit is made or (3) the fit is made to some function of the raw data, with the most common example being the exponential fit where the logarithms of the measured values are fitted [92]. The weighted regression procedure, with the correct weights, minimizes the sum of weighted squared residuals to produce residuals with a constant variance. In practice, the effect may not be obvious, but depending on the number of measurement points and associated error magnitudes, it may be significant.

Clearly stating the fitting procedure and the goodness of the fit is important to allow for comparison with other investigations. In this work, each calculated reaction rate has a measurement uncertainty and a standard deviation associated with fitting to the model for the time evolution of the NDD. Further, the exponential decay of the reaction rates is linearized according to Arrhenius-type behavior. By this two-step procedure to extract the activation energies, the need for careful investigation of the error propagation arises. Thus, the need for weighting in both steps will be considered in Section 4.2.

Chapter 4

Results and Discussion

The main aim of this work was to gain a further understanding of the complex LeTID defect mitigation. Accordingly, these measurements and calculation results constitute the main part of this chapter. Firstly, the accelerated LeTID mitigation results will be presented. This section includes the impact of a pre-DA step and the stability test results. The next section deals with the defect kinetics under a range of illumination intensities. A discussion of the need for weighted regression is included in this section to emphasize the importance of error propagation analysis in the procedure of extracting the activation energies. Finally, the chapter is concluded with spatial evaluations of the defect.

4.1 Accelerated Degradation and Regeneration Under 3 Suns Illumination

The evolution of carrier lifetime due to LeTID during two mitigation approaches was monitored periodically by incremental PL-I measurements. We applied 3 suns illumination to speed up the occurring degradation–regeneration cycle. **Group A** samples received LS treatment at a range of temperatures. **Group B** samples were dark annealed for 20 min at 200 or 300 °C before the LS treatment. The subsequent stability after the mitigation processes was tested in the regenerated state for both groups of samples. In general, the results show: (1) increasing annealing temperatures accelerate the LeTID mitigation, (2) a non-linear correlation between the maximum degradation extent and the annealing temperature, (3) the degradation–regeneration cycle does not seem to be considerably modulated after the pre-DA step at 200 °C, while the pre-DA step at 300 °C appears to reduce the degradation extent and slow the rate and (4) there seems to exist a threshold temperature as of which the completeness of the LeTID mitigation is compromised.

In the following subsections, these results will be explored in greater detail. Firstly, a general presentation and discussion on the temperature dependence of the degra-

dation and regeneration will be given. Secondly, a discussion on the impact of DA prior to accelerated LeTID mitigation under 3 suns illumination follows. Lastly, a comparison of the stability of samples treated at different temperatures with or without the DA step will be given.

4.1.1 Temperature dependence of the degradation and regeneration

Figure 4.1.1 presnts the evolution of the normalized effective lifetime of the **Group A** samples during accelerated degradation and regeneration treatment at 3 suns illumination and temperatures ranging from 100–300 °C. Since all samples are sister wafers and were processed together, they have a similar initial effective lifetime of $220 \pm 5\,\mu s$ (at $\Delta n \approx 2.2 \cdot 10^{15}\,cm^{-3}$). A stop criterion for the LS treatment duration was determined from a test experiment with sister samples to allow for a consecutive stability test starting in the regenerated state, which we will get back to in Section 4.1.3.

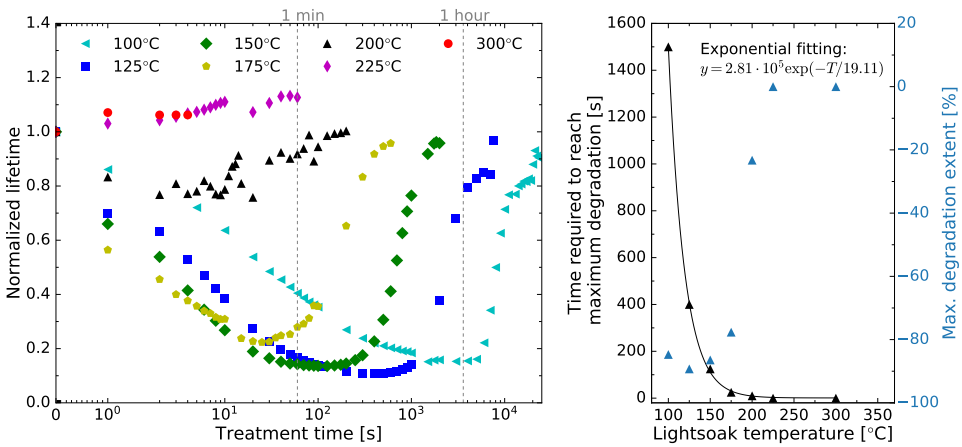

Figure 4.1.1: Left: Evolution of the normalized effective lifetime under 3 suns illumination as a function of accumulated LS time at elevated temperatures. The temperatures were varied between 100 and 300 °C. **Right:** Time required to reach the maximum degradation (minimum lifetime) and relative change in lifetime as a function of annealing temperature. The fitted correlation line is a guide for the eye.

Samples treated at 100–175 °C clearly show the expected decrease and subsequent recovery of the lifetime with further LS. In this temperature range, the degradation–regeneration curve shifts to shorter required treatment time for regeneration with increasing temperature, suggesting an acceleration of the reactions following Arrhenius-type behavior. The most severe degradation is found at 125 °C, and the amplitude of the lifetime loss is found to decrease with increasing temperatures above this temperature. None of the samples fully regenerate, and a relative lifetime decrease of 3–7 % is found with increasing temperatures, yielding a better

recovery. Only in this temperature range is it possible to determine the maximum degradation extent with certainty.

For the sample treated at 200 °C, a noisy measurement series is observed, while the degradation and subsequent regeneration are still visible. A "jump" in the amplitude decrease from 175 to 200 °C suggests that even a small change in sample temperature can make a big impact on the degradation-regeneration cycle at 200 °C. It should be noted that the precision of the hotplate was not ideal, and inhomogeneities across the plate and in time were found. A likely explanation for the noisy degeneration–regeneration cycle is then that the hotplate is not able to keep the sample at exactly 200 °C during the treatment. Another possible explanation is that the temporal resolution of measurements is too short for the sample to reach 200 °C during the treatment (this could apply to the samples treated at 225 and 300 °C as well). This contribution is believed to have a minor effect since the sample had to be placed on the hotplate before switching on the LED lamps, which takes a couple of extra seconds. This sample fully regenerates to its initial lifetime.

An immediate improvement in the lifetime is observed for the samples treated at 225 and 300 °C, which surpass the initial lifetime value by up to 13 %. This lifetime increase, or a part of it, could be due to the recovery of a small amount of meta-stable LeTID-related defects pre-formed during the simulated contact firing treatment [30, 93]. However, the beneficial effect of passivating the grain boundary recombination of charge carriers during firing has a significantly larger impact on the lifetime, preventing the determination of the amount of defects formed in this step. From the data, it is unclear whether the degradation–regeneration cycle occurred but was concealed by lack of temporal resolution and decreasing amplitude, or if it did not occur. This will be investigated in Section 4.1.3.

The treatment time needed to reach maximum degradation and the maximum degradation extent as a function of annealing temperature is shown in Figure 4.1.1. It is difficult to determine the exact time of the maximum degradation for the sample treated at 200 °C, but based on the test data and the trend for the other samples, it is believed to be at ~ 10 s. An exponential decay of the time to reach maximum degradation with the increase in temperature is found. Liu et al. [93] also found this relationship for DA. The exponential fit can be used to predict the LeTID kinetics for samples investigated with the same applied illumination and in the same temperature range.

Interestingly, the maximum degradation at 125 °C is higher than for 100 °C. A steep decrease in the maximum degradation extent is found in the temperature range 125–200 °C. The plateau for the two highest temperatures suggests that there exists a certain threshold temperature above which no degradation is observable. These results suggest a non-linear correlation between the maximum degradation extent and the annealing temperature, where the increasing temperature first leads to an increase and then a decline in degradation extent, in accordance with the study of Liu et al. [46]. This study speculated that degradation extent is correlated

with the defect precursor concentration present in the bulk of the silicon, possibly the varying concentration of boron–hydrogen bonds within the bulk of the silicon wafer [46].

Figure 4.1.2 presents PL images of the sample treated at 125 °C in three states: at the initial state, at the most degraded state and at the end of the LS process. Also shown are ratio images of the mean change with respect to the image before the LS treatment. An in-house MATLAB-script was used to process the images. The degradation seems relatively uniform, with two exceptions: (1) the most dislocated regions and grain boundaries and (2) the visible belt structure from the simulated contact firing in the belt furnace. (1) is consistent with the studies by Luka et al. [94] and Vargas et al. [35] under CID and DA conditions, respectively. (2) is consistent with the study by Niewelt et al. [95]. As discussed, the sample does not fully regenerate. The observed regeneration is also quite uniform, again with the exception of some dislocation clusters.

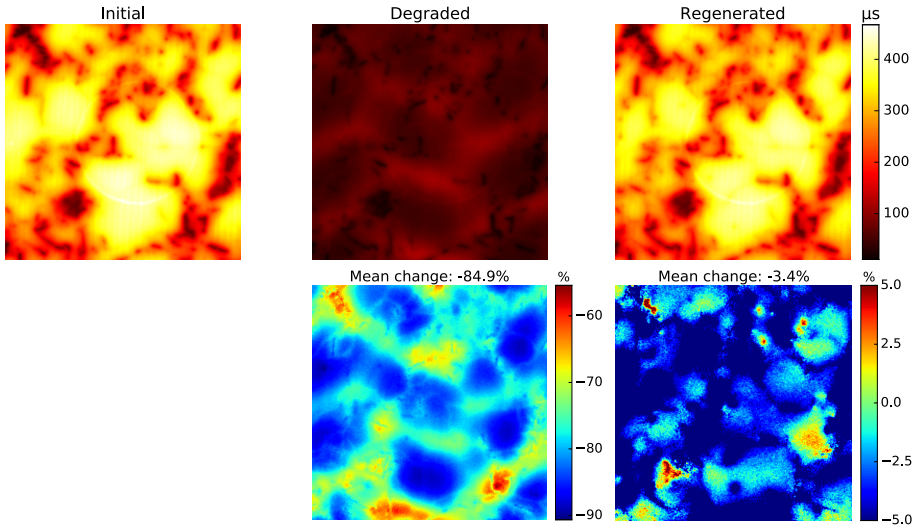

Figure 4.1.2: PL images of the sample treated at 125 °C in the initial, degraded and regenerated state along with the image ratio.

4.1.2 Impact of dark annealing prior to light soaking

To get a better understanding of the pre-DA impact on accelerated degradation and regeneration, two DA temperatures were investigated. The modulation of LeTID as a result of changing the pre-DA temperature is shown in Figure 4.1.3. To allow for easy comparison, the evolution of the normalized effective lifetime of respective samples in **Group A** are also shown with unfilled markers. Let us first consider the samples in **Group B**$_{200\,°\mathrm{C}}$.

These samples have higher initial lifetimes as compared to the wafers in **Group**

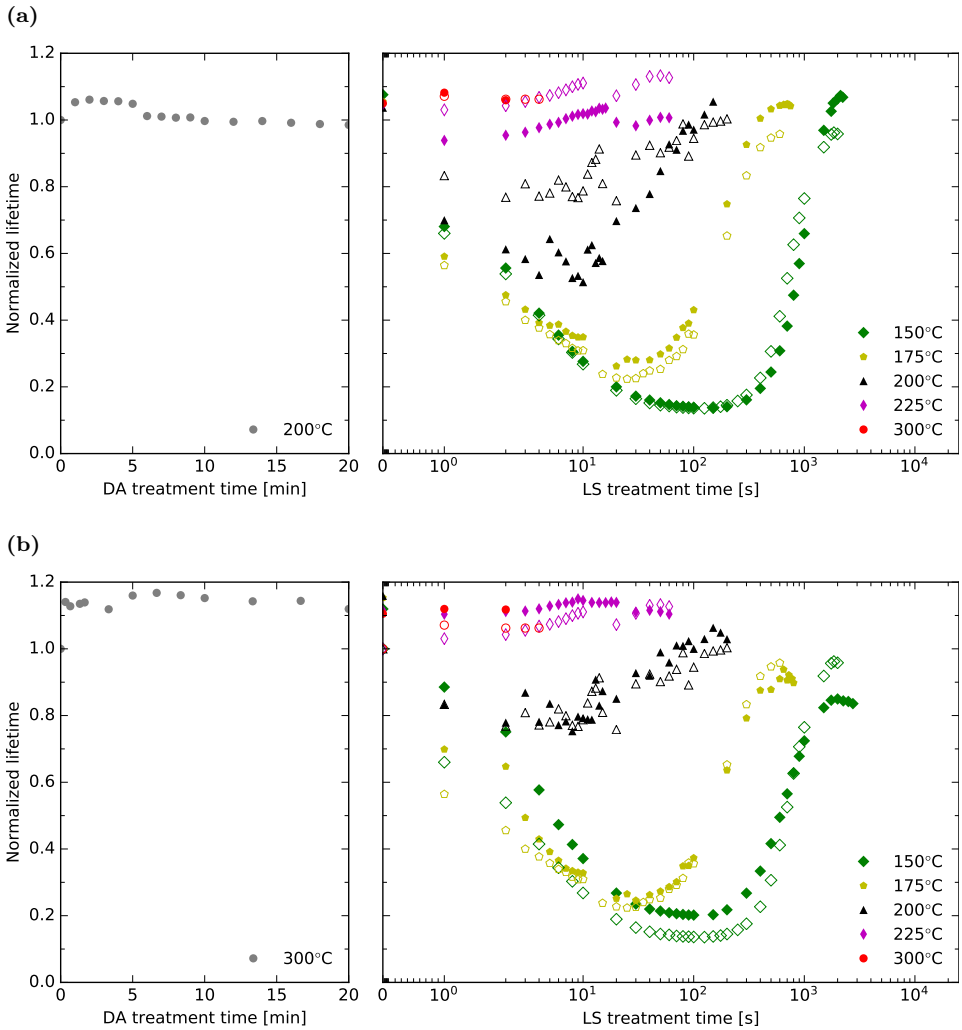

Figure 4.1.3: Evolution of the normalized effective lifetime during pre-DA at **(a)** 200 °C and **(b)** 300 °C with subsequent illumination under 3 suns. To allow for easy comparison, the evolution of the normalized effective lifetime of respective samples in **Group A** (no DA treatment) is also shown with unfilled markers.

A of $270 \pm 13\,\mu s$ (at $\Delta n \approx 2.2 \cdot 10^{15}\,cm^{-3}$). From Figure 4.1.3a, it is evident that the lifetime of the sister wafer monitored during pre-DA immediately increases and drops down to approximately the initial lifetime after 5 min. As the lifetime after the DA step shows a small increase for all other samples (τ=283 ± 16 µs), it is unclear what causes this drop. This behavior may indicate that the effects of intermittent cooldowns for measurements are not insignificant, or it may indicate added

scratches by sample handling. From the investigations of Chan et al. [7] and Vargas et al. [35], who studied non-compensated cells and wafers, we expected a small decrease in the lifetime during the first 10 minutes followed by a steeper degradation until 20 minutes is reached. A possible explanation for this is the different effects of B versus B–Ga co-doping and compensation, but other explanations may also account for this, e.g., the different impurity concentrations.

In general, modulation of the LeTID defect kinetics due to the pre-DA step at 200 °C is largely unnoticeable for the samples regenerated at 150, 175 and 300 °C. Closer inspection of the figure reveals that the degradation almost perfectly coincides with the samples regenerated at 150 °C. Still, the sample regenerated after pre-DA recovers at a slower rate. In addition, the lifetime is improved by 5 %. For the sample treated at 175 °C, the degradation extent is marginally reduced, and the regeneration rate is slightly increased. The lifetime is improved by 5 % for this sample as well. Since we are comparing neighbor wafers, these differences in the degradation–regeneration cycle could be due to minor variations in the grain structure and different initial lifetimes.

At first glance, it might appear that the pre-DA step at 200 °C dramatically changes the degradation–regeneration cycle for the samples regenerated at 200 and 225 °C. The degradation extent is indeed increased for these samples. However, as we already discussed, even a small change in sample temperature can make a considerable impact on the degradation–regeneration cycle in this temperature range. This contribution is believed to be dominant as temperature differences of $\sim 2\,^{\circ}\mathrm{C}$ were measured.

Turning now to consider the experimental evidence of the samples in **Group $\mathbf{B}_{300\,^{\circ}\mathrm{C}}$**, which have initial effective lifetimes of $284 \pm 4\,\mu\mathrm{s}$ (at $\Delta n = 2.2 \cdot 10^{15}\,\mathrm{cm}^{-3}$), it can be seen that the lifetime immediately increases and stays relatively stable in the pre-DA step. This is interesting: based on Vargas et al.'s study [35], we expected a close to linear increase in lifetime. After the pre-DA step, the samples have lifetimes of $322 \pm 3\,\mu\mathrm{s}$ (at $\Delta n = 2.2 \cdot 10^{15}\,\mathrm{cm}^{-3}$).

What stands out in Figure 4.1.3b is that the LeTID defect kinetics is modulated by this pre-DA treatment. This observation is especially evident for the samples treated at 150 and 175 °C. Significant degradation can be observed, but with reduced extents and slow rates as compared to the corresponding samples with no pre-DA. This is consistent with the results presented in [7, 35]. The sample regenerated at 150 °C has a lifetime decrease of 15 %, which is the highest decrease of all samples both in **Group A** and **B**. For the sample treated at 200 °C, it is hard to judge whether the LeTID characteristics are changed by pre-DA due to noisy measurement series. An immediate lifetime improvement, which exceeds the improvement for samples treated without the pre-DA step, is seen for the samples treated at 225 and 300 °C.

The most striking observation to emerge from the data comparison was that a 20 minutes pre-DA at 200 °C does not have a significant impact on the LeTID characteristics, while changing the pre-DA temperature to 300 °C reduces the degradation

extent and slow the rate. We hypothesize that a plausible explanation for the noisy measurement series seen for all samples light-soaked at 200 °C (with or without the pre-DA step) is that a different reaction path is taken around 200 °C. The large variation between each measurement point implies that a chemical complex either dissolves or arises at a distinct temperature. Such a complex can be, e.g., a dopant-hydrogen complex.

Having discussed two LeTID mitigation approaches, the final part of this section addresses the stability of these samples after regeneration.

4.1.3 Stability

Succeeding the first treatment step, aimed at mitigating LeTID for **Group A** and **B** samples, a stability test was initiated. However, the stability test had to be performed in two rounds, and some samples had to be omitted due to the limitation in space on the hotplate. The goal of the stability test was twofold: (1) to test the stability of the regenerated wafers that clearly showed the expected degradation–regeneration cycle during LeTID treatment and (2) to check whether the lifetime improvement is stable for the wafers that did not show the expected degradation–regeneration cycle. Thus, **Group A** wafers treated at 125–300 °C and **Group B** wafers treated at 150, 200 and 300 °C were chosen. This division ensured wafers with all three types of lifetime evolution: (1) the expected decrease and recovery of the lifetime, (2) a noisy decrease and recovery of the lifetime and (3) an immediate increase in lifetime. Figure 4.1.4 presents the stability test results. Note that the lifetime is now normalized with respect to the regenerated lifetime.

For all **Group A** treatment conditions with temperatures up to 200 °C, an increase in stability was observed in comparison to the non-treated sample. The residual losses could be explained by failure to stop the first treatment step at the time of maximum regeneration, causing a premature or overdue abortion before or after a sufficiently stable stage was reached. This explanation is supported by the observation that the sample regenerated at 125 °C seems to have continued the regeneration from the start of the stability test until the first lifetime measurement. Nevertheless, the magnitude of the residual losses is found to decrease with increasing maximum degradation extent in the first treatment step. This relationship suggests that the LeTID mitigation process is more effective for samples with high maximum degradation extent.

However, for the two highest temperatures, the samples prove to be unstable to a high degree. In fact, they degrade to the same extent as the non-treated sample. These results imply that the absence of a visible degradation–regeneration cycle during the first treatment step is not only due to lack of temporal resolution, but that the intended LeTID mitigation either did not occur or was insufficient in eliminating the defect to the desired degree.

In sum, these results show that increasing the temperature accelerates the process as desired, but it also leads to increasingly incomplete mitigation of LeTID. There seems to exist a threshold temperature above which the completeness and thereby

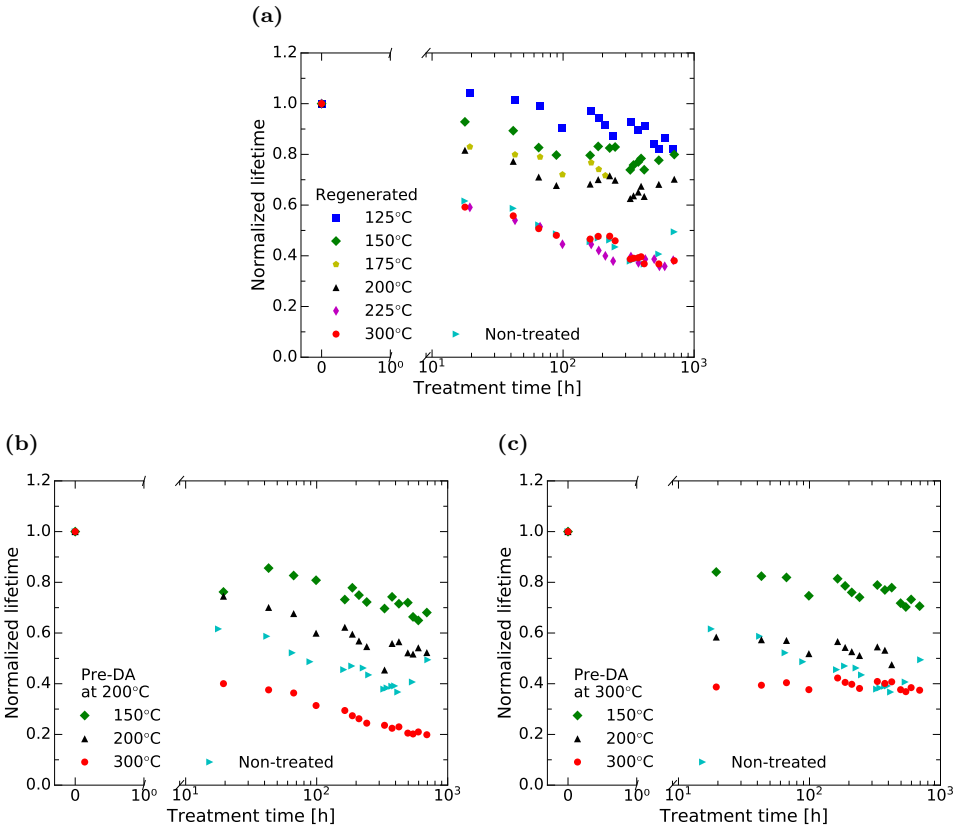

Figure 4.1.4: Stability test at 75–80 °C under illumination of 0.5–0.6 kW/m^2 after: **(a)** LS under 3 suns illumination, **(b)** 20 min DA at 200 °C followed by LS under 3 suns illumination and **(c)** 20 min DA at 300 °C followed by LS under 3 suns illumination. The lifetime is normalized with respect to the regenerated lifetime for all samples. In addition, the degradation and regeneration of a non-treated sample is shown. Note that the sample regenerated at 175 °C and the sample regenerated at 200 °C after the first DA step at 300 °C broke after 210 and 376 hours, respectively, and they were not measured again.

the stability is compromised. The results also indicate that a partial destabilization of the passivation and/or dissociation of defects may co-occur. Further, this implies that an accelerated degradation–regeneration process within industrially feasible treatment times might not be possible to implement.

Turning now to the results of **Group B**$_{200\,°C}$ samples in Figure 4.1.4b, it is evident that the samples regenerated at 150 and 200 °C show the same behavior as their counterparts in **Group A**. However, the residual losses are higher for these samples. A plausible explanation could, as we discussed above, be that the LS treatment is not stopped exactly when the maximum regeneration is reached. Surprisingly,

the sample treated at 300 °C degrade to a notably higher extent than both the non-treated sample and its counterpart in **Group A**, implying that the pre-DA step indeed negatively affected the LeTID mitigation.

If we now turn to the samples of **Group B**$_{300\,°\mathrm{C}}$ in Figure 4.1.4c, a quick onset of the residual loss can be observed. The residual losses are higher for these samples as compared to the respective samples in **Group A**. Beyond 20 hours, all the samples are quite stable. The sample treated at 300 °C degrades to a greater extent than the non-treated sample.

In this subsection, it has been explained that there seems to exist a certain temperature beyond which the LeTID elimination process becomes ineffective. This threshold temperature impedes the development of a fast post-processing LeTID mitigation by increasing the process temperature. Thus, the following section extends the study on the defect responsible for the LeTID degradation by investigating its kinetics as a function of temperatures at a range of illumination intensities.

4.2 Defect Kinetics

The spatially averaged QSSPC lifetime measurements of the **Group C** samples are used for the analysis in this section. The lifetimes were extracted at $\Delta n \approx 2.2 \cdot 10^{15}\,\mathrm{cm}^{-3}$. The samples were found to have a similar initial effective lifetime of $335 \pm 15\,\mu\mathrm{s}$. Section 3.5 describes the fitting methods used to estimate the reaction rates and activation energies presented in this section. As discussed in Section 4.1.1, the samples treated at temperatures exceeding 200 °C showed either a lot of noise or no observable degradation, making the analysis of reaction kinetics hardly possible. In addition, the light soaking system tended to turn off during the longer treatment intervals for the sample regenerated at 100 °C due to insufficient cooling of the LED lamps. Thus, for convenience, the illumination dependencies for the LeTID characteristics were investigated in the temperature range 125–175 °C.

In general, the results show: (1) a good fit between the experimental data and the model, (2) an approximately linear correlation between the reaction rates and the applied illumination, (3) a higher sensitivity to changes in treatment temperature than illumination intensity, (4) a decrease in defect formation activation energies for increasing illumination intensities and (5) no apparent trend for the regeneration activation energy.

In the following, these results will be presented more comprehensively. First, the overall dependency of reaction rates on illumination intensities and temperature are presented and discussed. Then, the extracted activation energies at several illumination intensities (0.5–3 suns) will be discussed and compared to literature values.

4.2.1 Reaction rates dependency of illumination and temperature

Only a single stage of lifetime degradation was observed for all investigation conditions. Thus, a single-exponential fit to the model proposed by Vargas et al. [35] (Equation (3.17)) was performed for all measured data. To illustrate the difference between the ordinary and weighted least squares method and to justify the choice of fitting method, the resulting fits to the NDD model under 3 suns illumination are shown in Figure 4.2.1. From Section 3.5.3, we remember that a relative uncertainty of 1–8 % is considered to be a good estimation for the uncertainty in lifetime [89]. We use the relative uncertainty mentioned above to estimate a 6 µs absolute uncertainty for our measured lifetimes. The lifetime uncertainty is used to calculate the weights for the weighted non-linear least squares fit to the NDD model through error propagation (error bars of the y-axis in Figure 4.2.1). As can be seen in the figure, the mean squared error (MSE) is closer to zero (perfect fit) for the ordinary least squares method than for the weighted least squares method, indicating that ordinary least squares gives the best fit for this data set and will accordingly be used in the following. Note that MSE values cannot be compared if the statistical methods used for estimating the unknown parameters in a model are not comparably complex. The ordinary and weighted least squares methods are considered to be quite similar even if the weighted least squares method is a bit more complex since the weights used need to be estimated. Both fits are good for temperatures 150–175 °C and have inequalities as compared to the experimental data for the sample treated at 125 °C, especially in the degradation part.

Figure 4.2.2 shows the NDD for the samples under LS at elevated temperatures along with the fits using ordinary non-linear least squares. In general, the NDD maximum amplitude increases at higher illumination intensities. However, with an intensity change from 2 to 3 suns illumination, the degradation extent drops a significant amount (up to 20 %) for the samples treated at 125 and 150 °C. A plausible explanation for this effect is the possible inadequate cooling of the LED lamps at 3 suns illumination and thus possible heating of the samples above the intended treatment temperature, which may impact the defect kinetics. Additionally, with an intensity change from 0.5 to 1 suns illumination, the degradation extent drops slightly for the samples treated at 125 and 175 °C; it is unclear what causes this drop. As we have already seen, the degradation extent is less severe for increasing temperatures.

The MSE of the fits is in the range $2.6 \cdot 10^{-8}$ to $4.5 \cdot 10^{-7}$, indicating a good fit between the experimental data and the model. Modest differences can be seen in the degradation part, while the fit is the poorest for the sample treated at 125 °C. These fits are consistent with Vargas et al.'s results and suggestion that the LeTID process can be described as a simultaneous degradation and regeneration process with different rates [35].

The illumination-dependent degradation and regeneration reaction rates are shown in Figure 4.2.3. We consider a 5 % uncertainty in the measured irradiance (error

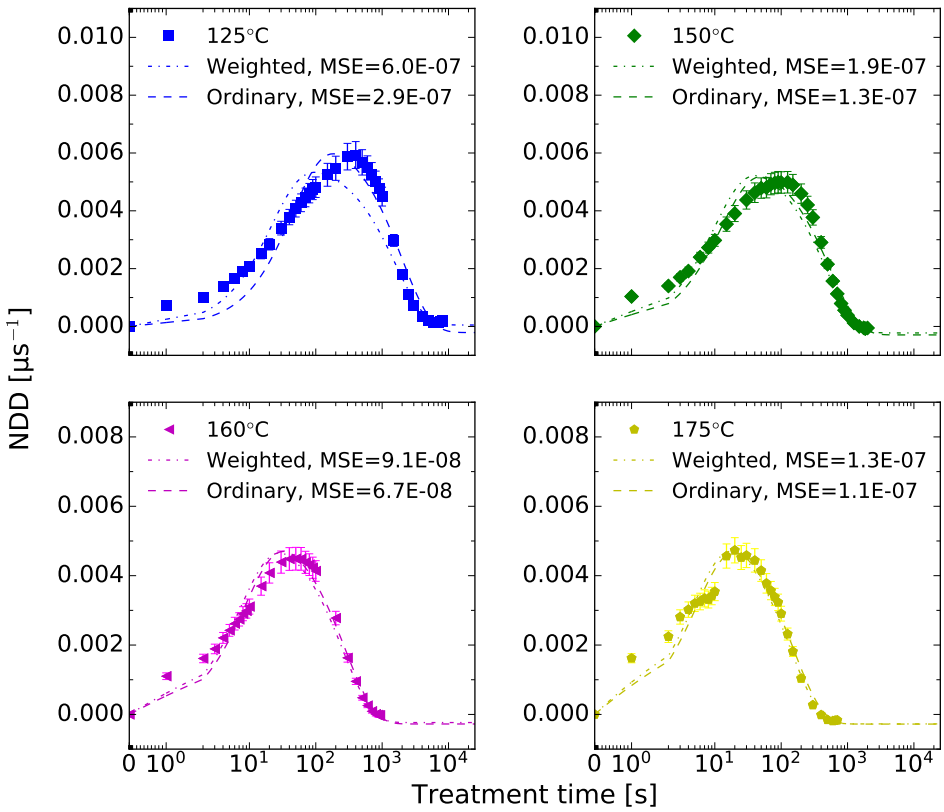

Figure 4.2.1: Time evolution of the NDD under 3 suns illumination. The plot illustrates the difference between the ordinary and weighted non-linear least squares fits.

bars of x-axis). The error bars of the y-axis are the standard deviation associated with the fitting of the reaction rates. It is evident from the figure that the rate of defect formation and regeneration is greatly enhanced by increasing the LS temperature. In general, both degradation and regeneration are accelerated by increasing the illumination intensity. The degradation rates at 160 °C stand out as the increase seems to saturate at 1 sun. However, this could be explained by the fact that the samples illuminated at 0.5–2 suns are from a neighboring position to the remaining sister samples in **Group C** (as we remember from Section 3.3.2, only 13 sister wafers were available for this investigation). A reasonable justification for this behavior is then that an additional non-negligible defect that is not only affected by the illumination is present in these three samples. Interestingly, this does not seem to affect the regeneration rates to the same extent.

The reaction rates show an approximately linear dependency on the applied illumination intensity, consistent with the observations of Bredemeier et al. [45] at low illumination intensities (0.25–1.5 suns) and of Liu et al. [46] at high illumination

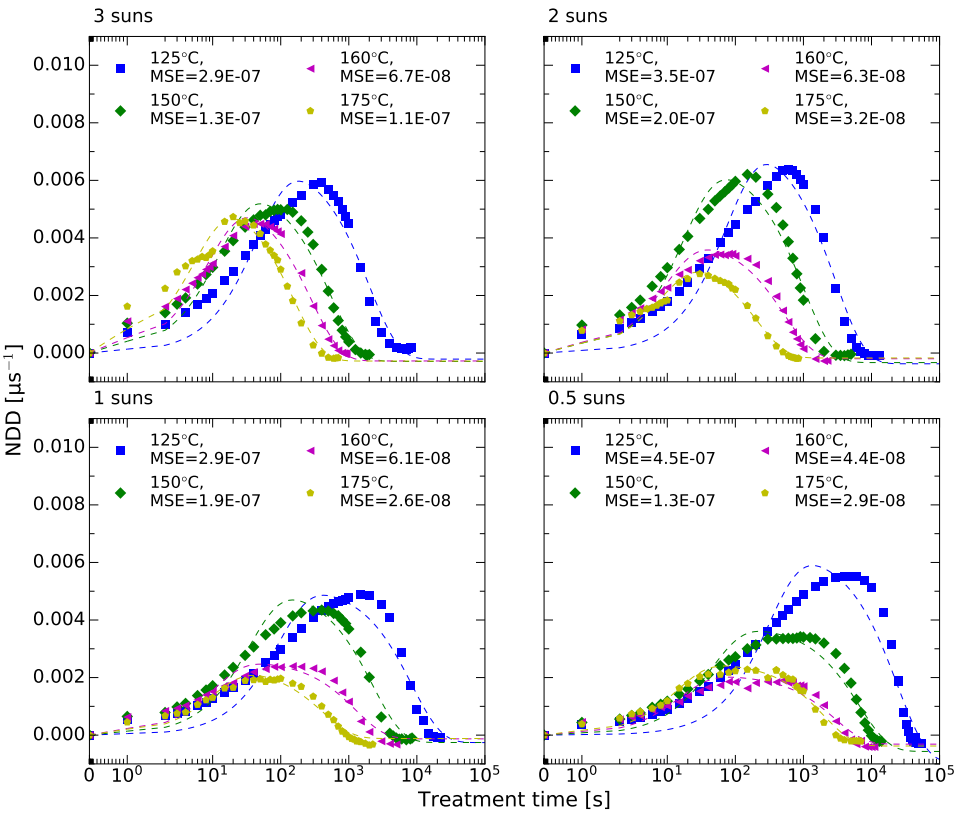

Figure 4.2.2: Time evolution of NDD along with non-linear least squares fits using Equation (3.17): Samples under LS at different temperatures and 3 suns, 2 suns, 1 sun or 0.5 suns illumination.

intensities (14.6–74.5 kW/m^2). In accordance with the present results, previous observations by Kwapil et al. concluded that this dependency is due to the linear correlation between the degradation rate constant and the excess carrier density (Δn) [47]. This suggests the involvement of one electron in the rate-limiting step of the defect formation [47]. The fitted reaction rate constants for both the degradation and regeneration reaction in the investigated range of temperatures support Kwapil et al.'s hypothesis. Further, the results are consistent with the suggestion that temperature plays a role in modulating the rate constant.

Figure 4.2.4 presents a contour plot of the maximum NDD distribution as a function of both treatment illumination intensities and temperatures investigated, where the x- and y-axes are the treatment temperature and illumination intensity, respectively. The color bar indicates the maximum NDD extent, with values interpolated between the 16 experimental data points. As can be seen from this plot, the maximum degradation extent of the investigated material is significantly more sensitive to changes in the processing temperature than illumination intensity. This depen-

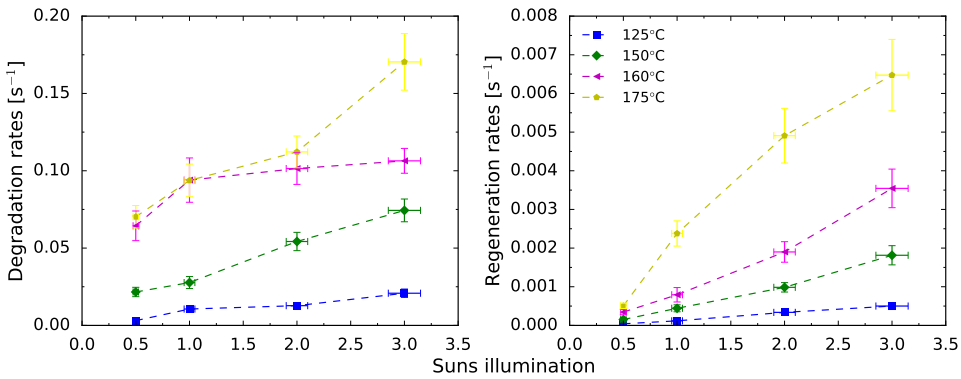

Figure 4.2.3: Degradation and regeneration rates as a function of illumination intensity at different temperatures. We consider a 5 % uncertainty in the measured irradiance (error bars of x-axis). The error bars in the y-direction indicate the standard deviation associated with the fitting. The dashed lines are guides for the eye.

dency was also found by Liu et al. under high illumination, but with a shift in the peak temperature [46]. In general, the maximum degradation extent happens at a treatment temperature of 125 °C for each illumination level tested. The highest NDD is found for treatment temperature 125 °C and 2 suns illumination.

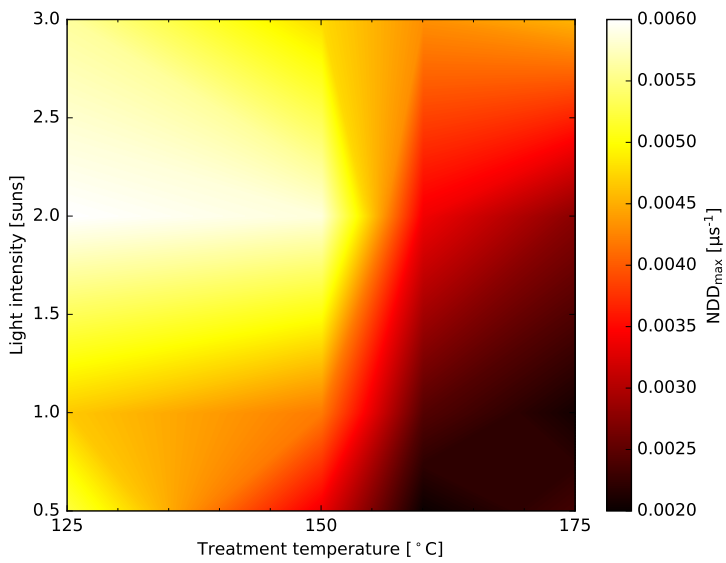

Figure 4.2.4: Contour plot of the $\mathrm{NDD_{max}}$ with values interpolated between the 16 experimental data points.

As we have discussed in this subsection, Figure 4.2.3 shows that increasing the LS temperature greatly enhances the reaction rates, while there is a lower increase

in the reaction rates with increasing illumination intensity. This indicates that it is possible to further accelerate the LeTID mitigation process by increasing the light intensity but not by increasing the temperature above about 200 °C, which we found to be the temperature beyond which the LeTID elimination process becomes ineffective in Section 4.1.3. It could be challenging to find an industrially relevant process for LeTID mitigation by post-processing with intensities of the magnitude examined here due to the time required. Liu et al. investigated illumination intensities that were an order of magnitude higher than in this work [46], which might sufficiently accelerate the mitigation process, but the stability was not studied. Thus, it is crucial to understand the root cause of the defect to avoid the degradation problem completely. In the remainder of this thesis, we will focus on finding clues to understand the root cause.

4.2.2 Activation energy at different illumination intensities

The activation energies under four different illumination intensities were compared to determine the illumination dependency of the energy level of the defect. As already mentioned, the degradation rates for the samples treated at 160 °C under 0.5–2 suns clearly show a different defect limiting lifetime than the rest of the samples. Further, it was shown that extracting the activation energies at 3 suns illumination without the measurement at 160 °C does not appreciably change the numerical value of the activation energies or the standard deviation of the fit. Thus, the reaction rates extracted at 160 °C will be omitted in the following.

In Figure 4.2.5, the degradation and regeneration rates are presented using an Arrhenius plot. By accounting for the measurement uncertainties in temperature and lifetime, and the standard deviation associated with fitting to the model for the time evolution of NDD, each reaction rate uncertainty was calculated by error propagation. In this relatively small temperature range, we consider a 2 °C absolute uncertainty in the measured temperatures. From Section 3.5.3, we remember that this error can be omitted in the least squares calculations since the uncertainty is equal for all temperatures. Thus, the error bars of the x-axis are not included in Figure 4.2.5. The plotted error bars of the y-axis are the standard deviation associated with the fitting to the model of the NDD time evolution.

Further, the reaction rate uncertainties were found to vary slightly from temperature to temperature. Accordingly, the weighted linear least squares method was used to fit the defect degradation and regeneration rates to the linearized Arrhenius equation (3.19), Figure 4.2.5 shows this plot. Note that the difference between the ordinary and weighted linear least squares method of extracting the activation energies was found to be within their respective measurement uncertainties. Hence, the effect of regression with the correct weights is not that obvious here, but, with more data points, it may be significant. Nevertheless, mathematically, the correct procedure is to use the weighted least squares method in this case.

Table 4.1 provides the extracted activation energies. Some selected literature values, which the activation energies estimated in this work, will be compared to can

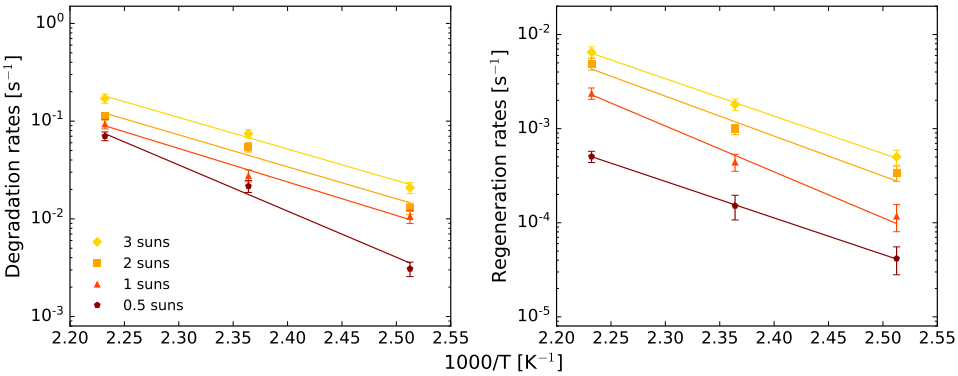

Figure 4.2.5: Arrhenius plot of the fitted reaction rate constants of the defect formation and mitigation at different illumination intensities plotted as a function of the inverse temperature ($1000/T$). The lines are fitted using weighted linear least squares and the plotted error bars of the y-axis are the standard deviation associated with the fitting to the model of the NDD time evolution.

Table 4.1: Estimated activation energies for different illumination intensities using weighted linear least squares.

Illumination [suns]	Deg. activation energy [eV]	Reg. activation energy [eV]
3	0.64 ± 0.05	0.79 ± 0.07
2	0.65 ± 0.04	0.84 ± 0.07
1	0.68 ± 0.06	0.97 ± 0.10
0.5	0.94 ± 0.06	0.77 ± 0.10

be found in Table 4.2. The defect formation activation energy was found to be in the range 0.64–0.94 eV and appears to have a steep decline with illumination intensity to a threshold value followed by a steady decrease for higher illumination levels. In accordance with the present results, Liu et al. found defect formation energies to have a tendency of decreased activation energies for higher illumination levels with values within the range of 0.62–0.78 eV when investigating irradiance levels ranging from 14.6–74.5 kW/m^2 [46]. The comparable activation energies for 1–3 suns in this work, and 30.5–74.5 eV in Liu et al.'s work [46], is interesting as the applied illumination intensity in the latter is an order of magnitude higher. As nearly every photon of both LEDs and lasers contribute to charge carrier generation, it is hypothesized that there exists a limit where higher illumination intensities do not contribute to the decrease in activation energy of defect formation. Interestingly, the activation energy at 0.5 suns illumination is within the uncertainty of the value extracted for the slow degradation ($E_{\text{deg, slow}} = 0.94 \pm 0.06$ eV) in Bredemeier et al.'s investigation [45]. Further, within the uncertainty, the activation energy at 3 suns illumination is equal to Zhou et al.'s study for for gallium co-doped p-type

Table 4.2: Selected literature values of the degradation and regeneration activation energies[1].

	Deg. activation energy [eV]	Reg. activation energy [eV]	Intensity/DA
Bredemeier et al. [45]	0.89 ± 0.04	–	0.5 suns
	0.94 ± 0.06		
Liu et al. [46]	0.78 ± 0.05	0.70 ± 0.04	$14.5\,\mathrm{kW/m^2}$
	0.64 ± 0.04	0.67 ± 0.02	$30.5\,\mathrm{kW/m^2}$
	0.63 ± 0.11	0.68 ± 0.02	$44.9\,\mathrm{kW/m^2}$
	0.62 ± 0.07	0.72 ± 0.03	$60.1\,\mathrm{kW/m^2}$
	0.62 ± 0.09	0.78 ± 0.08	$74.5\,\mathrm{kW/m^2}$
Vargas et al. [35]	1.08 ± 0.05	1.11 ± 0.04	DA
Zhou et al. [71]	0.65 ± 0.05	0.80 ± 0.04	7 suns

[1] Note that the illumination intensities listed here are the same as the ones used in the respective articles and do not correspond to the unit suns as defined in Section 3.3.1.

cast-mono Si PERC solar cells [71] using the same light soaker system as in this work. All activation energies are significantly lower than what Vargas et al. found for DA [35]. Additionally, all activation energies for higher illumination than 0.5 suns are lower than Bredemeier et al.'s result [45]. A possible explanation for the difference in calculated degradation activation energies is recombination enhanced defect reactions (REDR), which are known to decrease activation energies with increasing high injection levels [96–98]. Lattice vibrations caused by non-radiative capture of free carriers by a deep-level defect can significantly reduce the thermal activation energy [46]. Thus, reductions in activation energies with increasing illumination intensities could be expected.

The calculated regeneration activation energy was found to vary between 0.77–0.97 eV, but no obvious trend can be found in this data. All values are similar or even identical within their respective fitting and measurement uncertainties. An interesting observation is that the increase in illumination intensity only seems to affect the degradation, but not the regeneration activation energies of these samples. This result is in accordance with Liu et al.'s observations, who did not find an apparent trend and the values to be within the range 0.67–0.78 eV [46]. So it seems that higher illumination intensities indeed might be beneficial for regeneration, but, possibly due to the long timescales of regeneration, the increase needs to be significantly greater than the investigated range in this work. The activation energy at 3 suns illumination is within the measurement uncertainty equal to the value obtained by Zhou et al. [71].

Since the extracted activation energies are based on a relatively limited amount of data, further work is required to establish confidence in these values. Although, by comparing the results of this work to literature values, the extracted activation energies seem reasonable. However, as discussed in Section 3.3, an accurate com-

parison is not possible due to different ways of specifying the applied illumination intensity.

In this section, it has been explained that the degradation activation energy decrease with increasing illumination intensities and that no apparent trend could be found for the regeneration activation energies extracted in this work. The section that follows moves on to consider the spatial LeTID dependency.

4.3 Spatial LeTID Analysis

Having discussed the defect kinetics by analyzing the spatially averaged QSSPC lifetime measurements in Section 4.2, this section considers the spatially resolved PL measurements. Assessing the spatial variations across the wafer might give new insights into LeTID behavior. The samples analysed in this section are, as in Section 4.2, the **Group C** wafers. We limit ourselves to discuss the samples treated under 3 suns illumination here, but the same analysis can and has been applied to all illumination intensities. The analysis includes both local regions and single pixels considerations.

As already mentioned in Section 3.4, one should be aware of possible misinterpretations when using PL data and the NDD to compare the impact of LeTID in different regions of the sample. However, as we have seen in Section 4.2.1, these samples have a higher sensitivity to changes in temperature than illumination intensity. Thus, we assume that we have a similar relationship between the temperature and Δn. Assessing this assumption is considered to be beyond the scope of this work, so bear in mind that this is possibly a bold assumption that may not hold. A qualitative comparison of different regions and samples treated at different temperatures is regardless valid.

A more thorough spatial analysis can implement a countermeasure to avoid the possible misinterpretation due to the lack of truly injection-dependent lifetime data when comparing the lifetime obtained by PL-I in different grains. One could either combine measurements at various generation rates or adapt the generation rate individually for each grain. This will ensure that each grain features a similar luminescence flux and injection level.

4.3.1 Carrier lifetime images

Conventional PL images measured at certain stages of the defect formation and mitigation at room temperature and $\Delta n \approx 2.2 \cdot 10^{15}\,\mathrm{cm}^{-3}$ of the sample treated at 150 °C under 3 suns illumination are shown in Figure 4.3.1. Similar images were obtained for all treatment conditions, but they are not shown here. As we remember from Section 3.4, the effective lifetime is determined at a certain constant generation rate according to $G \cdot \tau_{\mathrm{eff}} = \Delta n \propto \Phi_{\mathrm{PL}}$ (Equation (3.16)). This means that we might as well have shown the Δn-images here. In this section, we consider trends as a function of the initial lifetime, but keep in mind that we would have seen identical trends if we had considered them as a function of initial Δn.

Some grain boundaries appear, but grains that are separated by less active grain boundaries can also be seen. Both small and larger dislocation clusters exist. Note that the degraded state is reached after 125 s, and the regenerated state is reached after 1850 s. We observe a severe lifetime degradation with a mean change of −83.8 %. The regeneration leads to a mean lifetime improvement of 6.5 %. During the process, the belt structure from the simulated contact firing in the belt furnace becomes visible as areas of higher lifetime. The belt structure is not visible in the regenerated state.

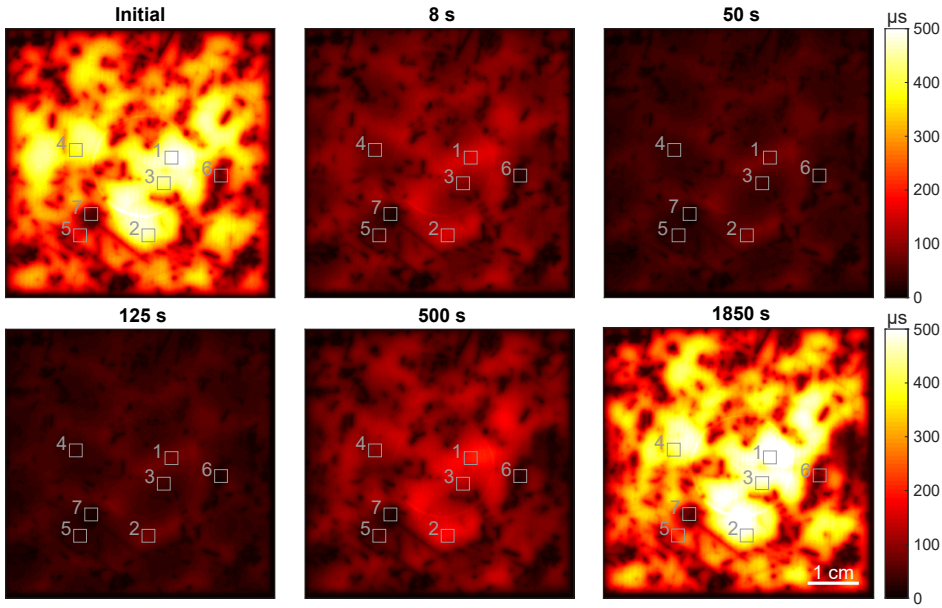

Figure 4.3.1: Spatially resolved lifetime maps measured at certain stages of the defect formation and mitigation of the sample treated at 150 °C under 3 suns illumination. Also shown is the local regions selected for the analysis in this section.

4.3.2 Local analysis

Seven local regions of 15×15 pixels, corresponding to $\sim 0.23 \times 0.23\,\mathrm{cm}^2$, as shown in Figure 4.3.1, were chosen for the analysis in this section. Regions 1–4 have high initial lifetimes, region 5 has a medium initial lifetime, while regions 6 and 7 include a small and a larger dislocation cluster, respectively, with low initial lifetimes.

The seven regions, with different initial lifetimes and grain structures, as indicated in Figure 4.3.1, were used to investigate the reaction rate and activation energy dependencies of the initial lifetime. Firstly, the observed lifetime behavior is different in the different regions, and the behavior is also strongly dependent on the

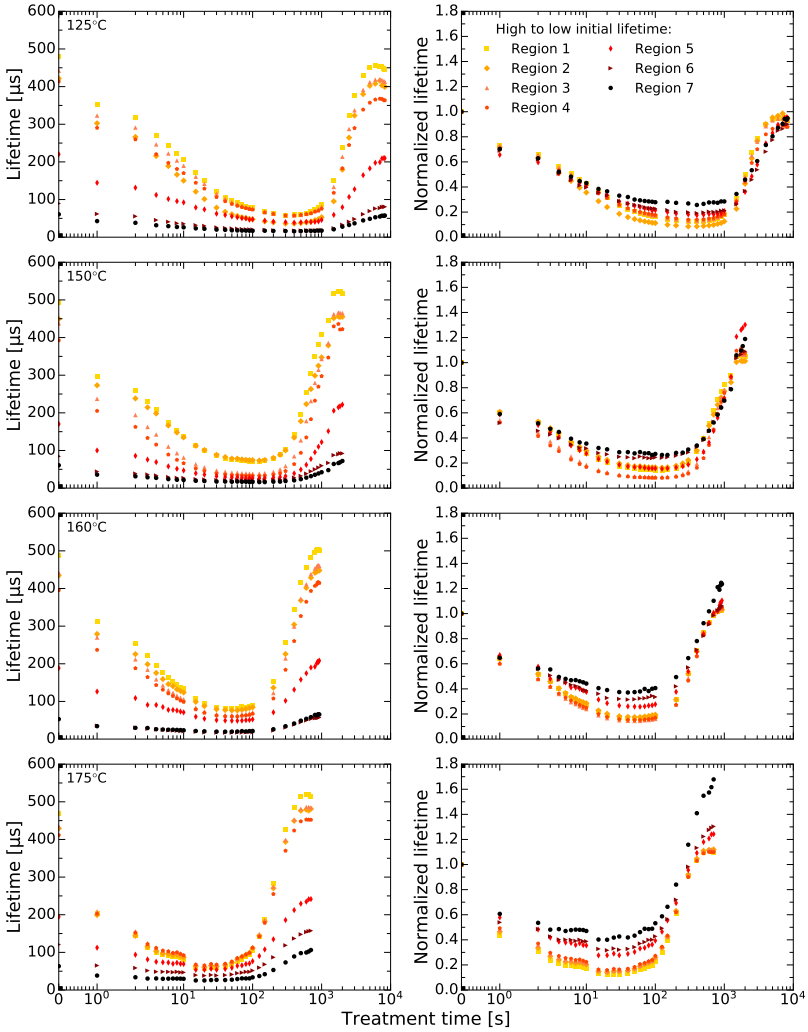

Figure 4.3.2: Evolution of the effective lifetime in seven regions under 3 suns illumination as a function of accumulated LS time.

treatment temperature, as seen in Figure 4.3.2. The NDD for the samples along with the fits using ordinary non-linear least squares are shown in Figure 4.3.3. In all cases, the modeled NDD curves show a good agreement with the experimental data, with generally better fits for high-lifetime regions. The MSE was found to be in the range $7.6 \cdot 10^{-8}$ to $1.9 \cdot 10^{-5}$. From Section 4.2, we expected the NDD maximum amplitude to decrease with increasing temperatures; this is not the case for all the regions as some of the high initial lifetime regions have the highest degradation extent for 150 °C. The time to reach the NDD maximum amplitude seems to be the same for all local regions within one sample.

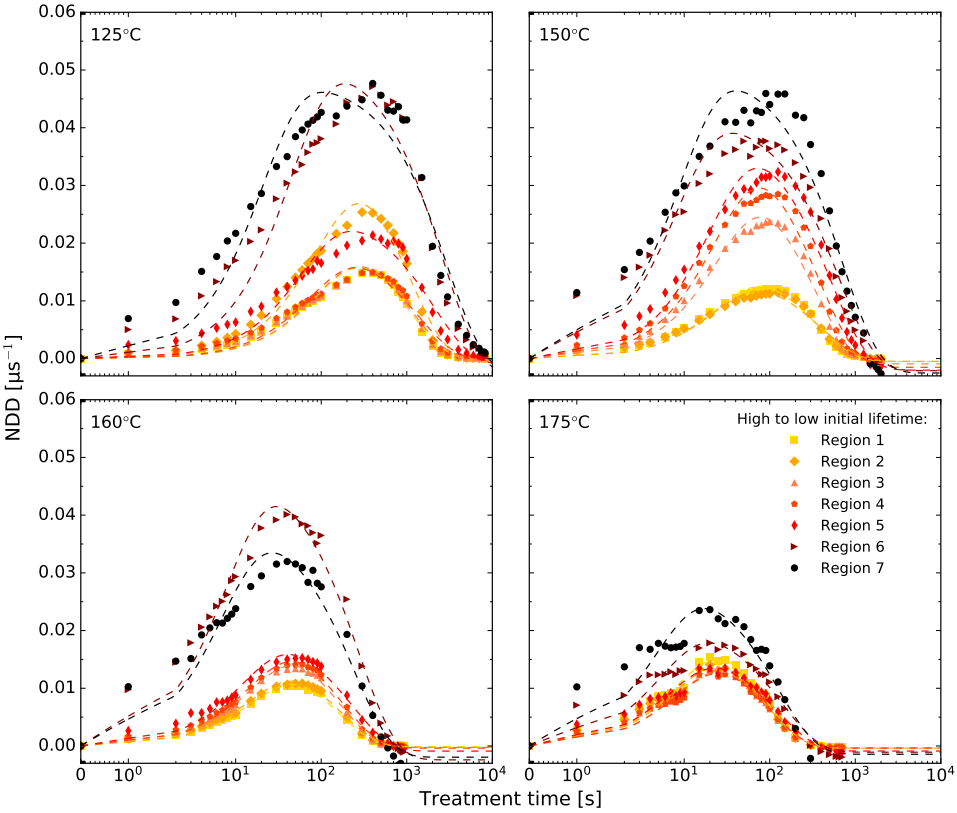

Figure 4.3.3: Time evolution of NDD in the selected regions along with non-linear least squares fits using Equation (3.17) under LS at 3 suns illumination.

Figure 4.3.4 shows the degradation and regeneration rates as a function of the initial lifetime in the seven local regions. As we have already seen in Section 4.2.1, increasing the treatment temperature enhances the rate of defect formation and regeneration. Further, the degradation rates seem to decrease, while the regeneration rates seem to increase as a function of the initial lifetime. If we assume that the bulk hydrogen is uniform across the wafer, the higher degradation rates for lower lifetimes may indicate that the degradation rates are impurity dependent. Gettering is, as we remember from Section 3.1.2.1, less effective in grain boundaries and dislocation clusters than in high-lifetime grains. Thus, gettering of impurities may explain the decreasing degradation reaction rates with increasing initial lifetime.

The local degradation and regeneration rates under 3 suns illumination in the different regions are presented using an Arrhenius plot, as seen in Figure 4.3.5. Table 4.3 provides the activation energies extracted from the plot. The degradation activation energy was found to be in the range 0.43–0.74 eV. This local analysis

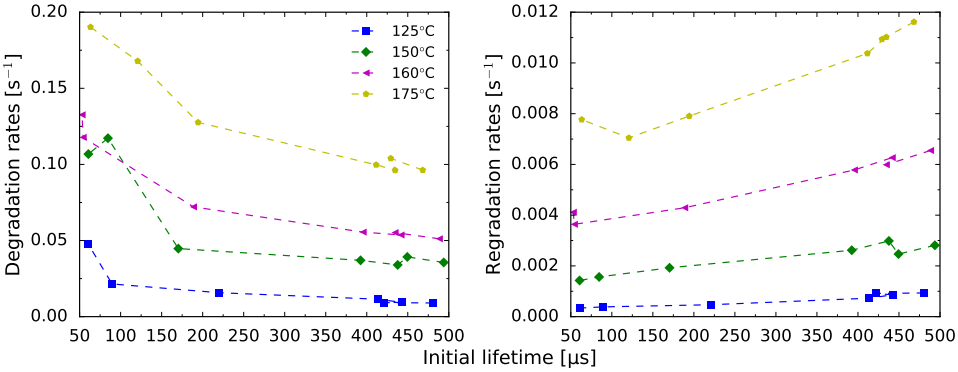

Figure 4.3.4: Degradation and regeneration reaction rates in the seven local regions under 3 suns illumination as a function of the initial lifetime. The dashed lines are guides for the eye.

suggests that the degradation activation energy increases as a function of the initial lifetime. Region 7 has a notably lower degradation activation energy compared to the other regions, but it is unclear if this is caused by a poor fit to the experimental data or can be explained by other means. The regeneration activation energy was found to fall within the range 0.78–0.99 eV and seems to be decreasing with increasing initial lifetime.

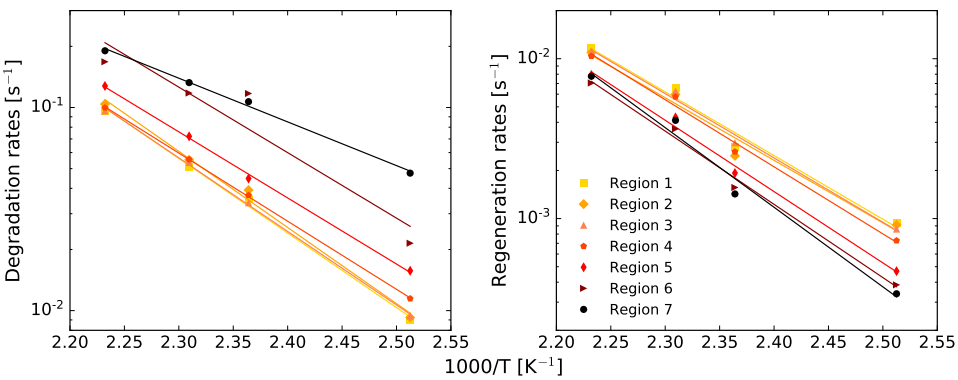

Figure 4.3.5: Arrhenius plot of the fitted reaction rate constants of the defect formation and mitigation in seven regions plotted as a function of the inverse temperature ($1000/T$).

Values from this local analysis can be compared with the values obtained in the spatially averaged QSSPC lifetime analysis. In Section 4.2.2, the activation energies were found to be 0.64 ± 0.05 eV for the degradation and 0.79 ± 0.07 eV for the regeneration. Since this local analysis indicates lifetime-dependent activation energies, the comparison of numerical values between the local and spatially averaged analysis should be done for comparable initial lifetimes. None of the regions have the same initial lifetime as the spatially averaged initial lifetime (335 ± 15 µs).

Table 4.3: Estimated activation energies for different regions in the sister samples under 3 suns illumination.

Region	Deg. activation energy [eV]	Reg. activation energy [eV]
1	0.73 ± 0.03	0.79 ± 0.08
2	0.74 ± 0.04	0.78 ± 0.09
3	0.72 ± 0.02	0.80 ± 0.05
4	0.67 ± 0.01	0.83 ± 0.06
5	0.65 ± 0.02	0.89 ± 0.05
6	0.64 ± 0.15	0.91 ± 0.06
7	0.43 ± 0.02	0.99 ± 0.09

Regions 4 and 5 have the closest initial lifetimes and are also found to have comparable activation energies to the values obtained in the spatially averaged QSSPC lifetime analysis.

Having considered local regions, we extend the same analysis to consider individual pixels separately.

4.3.3 Pixelwise analysis

For simplicity, a single row of 251 pixels approximately in the middle of the samples was chosen for the pixelwise analysis. A more comprehensive investigation could include all pixels or use a selection criterion, e.g., a desired maximum MSE of the fit, to choose which pixels should be included in the analysis. Figure 4.3.6 shows a stacking approach that combines single rows of the 251 pixels from each of the 35 PL images of the sample treated at 150 °C into one contour plot (i.e., a sequence of rows with values interpolated between the experimental data points) used to illustrate the lifetime evolution of the chosen pixels during the treatment.

Figure 4.3.7 shows the degradation and regeneration rates as a function of the initial lifetime in the pixels. It is apparent from the figure that the degradation rates decrease as a function of initial lifetime, while the regeneration rates increase as a function of the initial lifetime. These pixelwise results support the suggestion that the degradation rate is impurity dependent and that the regeneration is injection-level dependent. Note that all pixels have initial lifetimes close to or higher than 100 µs, the local analysis covered lower initial lifetimes (from approximately 60 µs). The reaction rate values are comparable to the rates calculated in the local regions (Figure 4.3.4).

The extracted degradation and regeneration activation energies in each pixel are shown in Figure 4.3.8. No obvious trend can be found in this data. Thus, the activation energies seem not to vary with the initial lifetime in the pixels; analyzing more pixels could add confidence to this suggestion. As the activation energy can be thought of as the magnitude of the energy barrier for a chemical transformation,

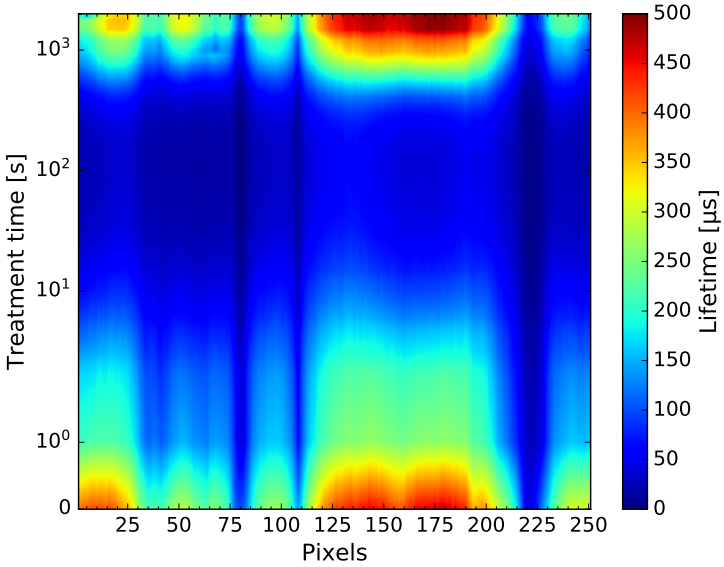

Figure 4.3.6: Contour plot of the lifetime evolution of the selected row of pixels during the treatment with values interpolated between the experimental data points.

it seems reasonable that the activation energy should primarily be related to the nature of the defect involved. A comparison of the pixelwise activation energies with the values obtained in the spatially averaged lifetime analysis reveals that the two approaches seem to give comparable results. The local activation energies in region 1–6 are found to be within the range calculated for the individual pixels. None of the pixels have as low degradation or high regeneration activation energy as region 7, but none of the pixels have a comparable low initial lifetime either.

In this section, we have shown that the reaction rates have the same trend in the local regions as the individual pixels. The degradation rates were found to decrease, while the regeneration rates were found to increase as a function of the initial lifetime. Further, no obvious trend was found for the activation energies, which are considered to be independent of the initial lifetime.

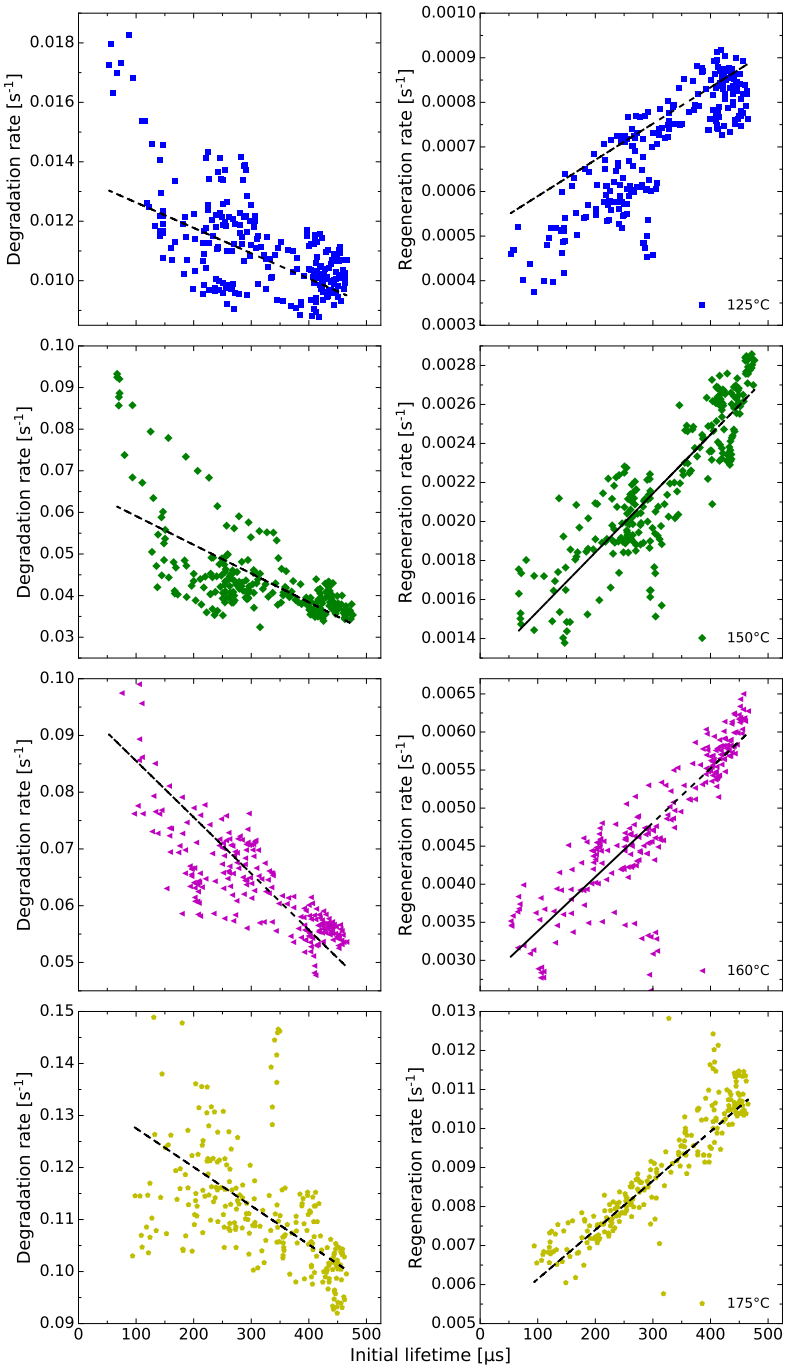

Figure 4.3.7: Degradation and regeneration reaction rates as a function of the initial lifetime in pixels. The dashed lines are fitted using ordinary least squares regression.

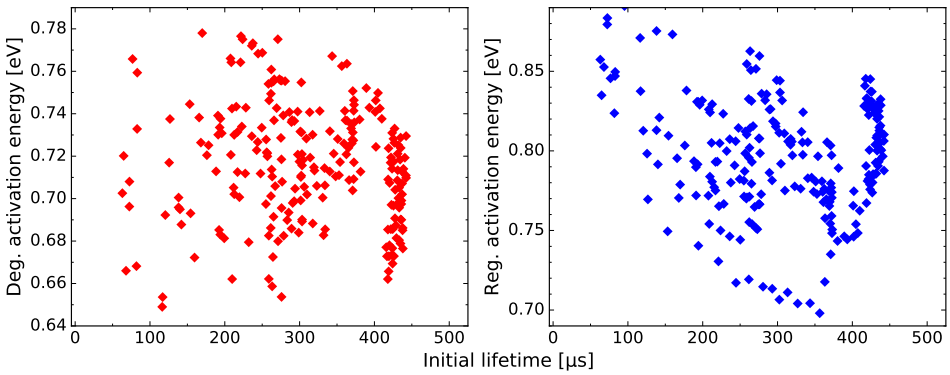

Figure 4.3.8: Extracted degradation and regeneration activation energies as a function of the initial lifetime in pixels.

Chapter 5

Conclusion

In this investigation, the aim was to gain a further understanding of the complex LeTID defect mitigation in p-type HPMC-Si and attempt to understand the root cause. This was done by investigating commercially available boron–gallium co-doped, compensated HPMC-Si wafers. The study was conducted by six steps: (1) studying the accelerated degradation and regeneration at 3 suns illumination and a range of temperatures, (2) investigating the impact of dark annealing prior to accelerated degradation and regeneration, (3) testing the stability of regenerated wafers, (4) examining the reaction rates dependency of the illumination intensity, (5) extracting the activation energy and ultimately (6) assessing the spatial variations in LeTID behavior.

To suppress the negative impact of LeTID, a regeneration treatment at elevated temperature (100–300 °C) under 3 suns illumination was applied to speed up the occurring degradation–regeneration cycle. It was shown that increasing the annealing temperature accelerates the LeTID mitigation as expected. Further, a non-linear correlation between the maximum degradation extent and the annealing temperature was found. For temperatures higher than 200 °C, it was unclear whether the degradation occurred during the process, but it lead to a slight improvement in the effective lifetime as compared to the initial value.

Investigations into the impact of a 20 min pre-DA step at 200 or 300 °C before the accelerated LeTID-treatment revealed differences in the resulting behavior. The degradation–regeneration cycle does not seem to be considerably modulated after the pre-DA step at 200 °C. In contrast, the pre-DA step at 300 °C appears to reduce the degradation extent and slow the reaction rates.

A subsequent stability test of the samples in the regenerated state revealed that samples treated at temperatures 125–200 °C proved to be rather stable, while LeTID still occurs for the samples treated at higher temperatures. Accordingly, higher temperatures, on one hand, accelerate the mitigation process as desired, but on the other hand, higher temperatures lead to systematically incomplete elimina-

tion of the defect. There seems to exist a threshold temperature above which the completeness of the LeTID mitigation is compromised. Further, the samples treated with the pre-DA step at 200 °C show a gradual decline in the measured lifetime with higher residual losses than the samples regenerated without the DA step. In contrast, the samples treated with the pre-DA step at 300 °C show a quick onset of the residual loss, after which the samples are quite stable.

The illumination intensity dependencies on the reaction rate of the LeTID defect formation and regeneration were investigated. A previously proposed model was used to calculate the reaction rates, and the need for weighted least squares regression was assessed. The model gives good approximations for temperatures 150–175 °C and an adequate fit for the sample treated at 125 °C using ordinary least squares regression. An approximately linear correlation between the reaction rates and the applied illumination intensity was found.

Based on the extracted rates, the Arrhenius degradation and regeneration activation energies were found to be between 0.64–0.94 eV and 0.77–0.97 eV, respectively. The degradation activation energy was found to decrease with increasing illumination intensities, while no apparent trend was found for the regeneration activation energy.

Finally, the spatial evaluation revealed that the reaction rates show the same trend in local regions as individual pixels. The degradation rates were found to decrease, while the regeneration rates were found to increase as a function of the initial lifetime. Further, the reaction rate trends were suggested to be due to an impurity and an injection level dependency for the degradation and regeneration rates, respectively. No obvious trend was found for the activation energies, which were therefore considered to be independent of the initial lifetime.

These findings provide additional information regarding the kinetics and properties of the LeTID-defect in *p*-type HPMC-Si wafers. This additional insight can contribute to the progress in the development of robust engineering solutions to improve the PERC on mc-Si substrates properties. It could be challenging to find an industrially relevant process for LeTID mitigation by post-processing, at least with the intensities of the magnitude examined here, due to the time required. Hopefully, the kinetics and the spatial evaluation can contribute to a further understanding of the defect so that it can be avoided.

Chapter 6

Further Work

Extending the LeTID investigation of industry-standard boron–gallium co-doped, compensated HPMC-Si wafers beyond the scope of this thesis can be done in several ways. Different approaches can either strengthen or falsify the statements made here. In this chapter, a few suggestions on how a more thorough understanding can be reached will be given.

A more extensive sample series, including non-compensated boron-doped mc-Si wafers with comparable resistivity, could be useful to truly differentiate the LeTID behavior in boron–gallium co-doped, compensated HPMC-Si from that in standard non-compensated material. This would constitute a solid foundation for making statements about the effect of ESS™ versus conventional Siemens feedstock. Additionally, it would be interesting to study LeTID in non-compensated boron-doped, gallium-doped and phosphorus-doped mc-Si wafers with comparable resistivity to assess whether the noisy measurement series seen at 200 °C is caused by a dopant-hydrogen complex that either dissolves or arises at a distinct temperature.

A more elaborate investigation of the NDD model is suggested. Modifications to the model or a different model may minimize the differences between the model and the experimental data for the degradation part of the curve, and give better fit especially for the sample treated at 125 °C. This will in turn increase the confidence in the calculated reaction rates. An easy workaround is to design the experiment so that only temperatures with better fits to the model is used, but this limits the investigation to a very small temperature range for these particular wafers and the light soaker used. Thus, this solution is discouraged. One could also assess whether surface-related degradation needs to be considered in the NDD model.

Bibliography

[1] United Nations. Sustainable Development Goals, 2016.

[2] Fraunhofer ISE. Photovoltaics report, updated: 14. November 2019.

[3] K. Ramspeck, S. Zimmermann, H. Nagel, A. Metz, Y. Gassenbauer, B. Birkmann, and A. Seidl. Light induced degradation or rear passivated mc-Si solar cells. In *European Photovoltaic Solar Energy Conference*, pages 861 – 865, 2012.

[4] F. Kersten, P. Engelhart, H.-C. Ploigt, A. Stekolnikov, T. Lindner, F. Stenzel, M. Bartzsch, A. Szpeth, K. Petter, J. Heitmann, and J. W. Müller. Degradation of multicrystalline silicon solar cells and modules after illumination at elevated temperature. *Solar Energy Materials and Solar Cells*, 142:83–86, 2015.

[5] D. N. R. Payne, C. E. Chan, B. J. Hallam, B. Hoex, M. D. Abbott, S. R. Wenham, and D. M. Bagnall. Rapid passivation of carrier-induced defects in p-type multi-crystalline silicon. *Solar Energy Materials and Solar Cells*, 158:102–106, 2016.

[6] P. P. Altermatt, Z. Xiong, W. He, Q.and Deng, F. Ye, Y. Yang, Z. Chen, Y.and Feng, P. J. Verlinden, A. Liu, D. H. Macdonald, T. Luka, D. Lausch, M. Turek, C. Hagendorf, H. Wagner-Mohnsen, J. Schön, W. Kwapil, F. Frühauf, O. Breitenstein, E. E. Looney, T. Buonassisi, D. B. Needleman, C. M. Jackson, A. R. Arehart, S. A. Ringel, K. R. McIntosh, M. D. Abbott, B. A. Sudbury, C. Zuschlag, A.and Winter, D. Skorka, G. Hahn, D. Chung, B. Mitchell, P. Geelan-Small, and T. Trupke. High-performance p-type multicrystalline silicon (mc-Si): Its characterization and projected performance in PERC solar cells. *Solar Energy*, 175:68–74, 2018.

[7] C. Chan, T. H. Fung, M. Abbott, D. Payne, A. Wenham, R. Hallam, B.and Chen, and S. Wenham. Modulation of Carrier-Induced Defect Kinetics

in Multi-Crystalline Silicon PERC Cells Through Dark Annealing. *Solar RRL*, 1(2):1600028, 2017.

[8] F. Kersten, F. Fertig, K. Petter, B. Klöter, E. Herzog, M. B. Strobel, J. Heitmann, and J.W. Müller. System performance loss due to LeTID. *Energy Procedia*, 124:540–546, 2017.

[9] A. Zuschlag, D. Skorka, and G. Hahn. Degradation and regeneration in mc-Si after different gettering steps. *Progress in Photovoltaics: Research and Applications*, 25(7):545–552, 2017.

[10] VDMA. 11th, International Technology Roadmap for Photovoltaics, 2020.

[11] H. Luo, L. He, Q. Lei, Y. Xu, S. Rao, C. Zhou, W. Mao, J. Li, X. Cheng, and G. Zou. Study on preparation and properties of boron-gallium co-doped multicrystalline ingots. *Journal of Crystal Growth*, 546:125784, 2020.

[12] S. Rein. *Lifetime spectroscopy - A method of defect characteruzation in silicon for photovoltaic applications.* Springer Berlin Heidelberg, Berlin, 2005.

[13] A. G. Aberle. *Crystalline silicon solar cells - Advanced surface passivation and analysis.* Centre for Photovoltaic engineering, University of New South Wales, 1999.

[14] D. K. Schroder. *Semiconductor material and device characterization.* Wiely, Hoboken, 2006.

[15] A. Smets, K. Jäger, O. Isabella, R. Van Swaaij, and M. Zeman. *Solar Energy.* UIT Cambridge Ltd, England, 2016.

[16] J. Nelson. *The physics of solar cells.* Imperial College Press, London, 2003.

[17] P. Würfel. *Physics of Solar Cells.* Wiely, Weinheim, 2005.

[18] K. Adamczyk. *Defect-impurity interactions in high performance multicrystalline silicon.* PhD thesis, Norwegian University of Science and Technology, Faculty of Natural Sciences, Department of Materials Science and Engineering, 10 2018.

[19] Formation of a pn-junction. `https://www.pveducation.org/pvcdrom/pn-junctions/formation-of-a-pn-junction`. Accessed: 2019-11-04.

[20] T. Trupke, M. A. Green, P. Würfel, P. P. Altermatt, A. Wang, J. Zhao, and R. Corkish. Temperature dependence of the radiative recombination coefficient of intrinsic crystalline silicon. *Journal of Applied Physics*, 94(8):4930–4937, 2003.

[21] H. Haug. *New methods for investigation of surface passivation layers for crystalline silicon solar cells.* PhD thesis, University of Oslo, Faculty of Mathematics and Natural Sciences, Department of Physics, 3 2014.

[22] W. Shockley and W. T. Read. Statistics of the recombinations of holes and electrons. *Physical Review*, 87(5):835–842, 1952.

[23] R. N. Hall. Electron-hole recombination in germanium. *Physical Review*, 87(2):387–387, 1952.

[24] J. O. Odden, T. C. Lommasson, M. Tayyib, J. Vedde, T. Buseth, K. Friestad, H. Date, and R. Tronstad. Results on performance and ageing of solar modules based on Elkem Solar Silicon (ESS™) from installations at various locations. *Solar Energy Materials and Solar Cells*, 130:673–678, 2014.

[25] A.-K. Søiland, M. G. Dolmen, J. Heide, U. Thisted, G. Halvorsen, G. Ausland, K. Friestad, P. Preis, K. Peter, O. Graf, T. Bartel, and R. Tronstad. First results from a simplified elkem solar route—input to tolerance limits. *Solar Energy Materials and Solar Cells*, 130:661–667, 2014.

[26] F. A. Trumbore. Solid solubilities of impurity elements in germanium and silicon. In *Bell System Technical Journal*, volume 39, pages 205–233, 1960.

[27] A-K. Søiland, J. O. Odden, B. Sandberg, K. Friestad, J. Håkedal, E. Enebakk, and S. Braathen. Solar silicon from a metallurgical route by Elkem Solar - a viable alternative to virgin polysilicon. In *CSSC-6*, Aix-Les-Bains, France, 2012.

[28] M. Tayyib, J. O. Odden, E. H. Dahl, P. Baggethun, and T. O. Sætre. Elkem Silicon vs polysilicon: A quantitative impurity element analyses. In *28th European Photovoltaic Solar Energy Conference and Exhibition*, Paris, France, 2013.

[29] S. Uda, X. Huang, M. Arivanandhan, and R. Gotoh. Enhancement of Ga doping in Czochralski-grown Si crystal by B- codoping. In *Int. Symp. Adv. Sci. Technol. Silicon Mater*, Kona, Hawaii, 2008.

[30] D. Chen, K. Moonyong, B. V. Stefani, B. J. Hallam, M. D. Abbott, C. E. Chan, R. Chen, D. N. R. Payne, N. Nampalli, A. Ciesla, T. H. Fung, K. Kim, and S. R. Wenham. Evidence of an identical firing-activated carrier-induced defect in monocrystalline and multicrystalline silicon. *Solar Energy Materials and Solar Cells*, 172:293–300, 2017.

[31] T. Niewelt, M. Selinger, N. E. Grant, W. Kwapil, J. D. Murphy, and M. C. Schubert. Light-induced activation and deactivation of bulk defects in boron-doped float-zone silicon. *Journal of Applied Physics*, 121(18):185702, 2017.

[32] H. C. Sio, H. Wang, Q. Wang, C. Sun, W. Chen, H. Jin, and D. Macdonald. Light and elevated temperature induced degradation in p-type and n-type cast-grown multicrystalline and mono-like silicon. *Solar Energy Materials and Solar Cells*, 182:98–104, 2018.

[33] M. A. Jensen, A. E. Morishige, J. Hofstetter, D. B. Needleman, and T. Buonassisi. Evolution of LeTID Defects in p-Type Multicrystalline Silicon During Degradation and Regeneration. *IEEE Journal of Photovoltaics*, 7(4):980–987, 2017.

[34] T. H. Fung, C. E. Chan, B. J. Hallam, D. N. R. Payne, M. D. Abbott, and S. R. Wenham. Impact of annealing on the formation and mitigation of carrier-induced defects in multi-crystalline silicon. *Energy Procedia*, 124:726–733, 2017.

[35] C. Vargas, G. Coletti, C. Chan, D. Payne, and Z. Hameiri. On the impact of dark annealing and room temperature illumination on p-type multicrystalline silicon wafers. *Solar Energy Materials and Solar Cells*, 189:166–174, 2019.

[36] K. Nakayashiki, J. Hofstetter, A. E. Morishige, T. A. Li, D. B. Needleman, M. A. Jensen, and T. Buonassisi. Engineering Solutions and Root-Cause Analysis for Light-Induced Degradation in p-Type Multicrystalline Silicon PERC Modules. *IEEE Journal of Photovoltaics*, 6(4):860–868, 2016.

[37] C. Vargas, K. Kim, G. Coletti, D. Payne, C. Chan, S. Wenham, and Z. Hameiri. Carrier-Induced Degradation in Multicrystalline Silicon: Dependence on the Silicon Nitride Passivation Layer and Hydrogen Released During Firing. *IEEE Journal of Photovoltaics*, 8(2):413–420, 2018.

[38] M. Padmanabhan, K. Jhaveri, R. Sharma, P. K. Basu, S. Raj, J. Wong, and J. Li. Light-induced degradation and regeneration of multicrystalline silicon Al-BSF and PERC solar cells. *physica status solidi (RRL) – Rapid Research Letters*, 10(12):874–881, 2016.

[39] M. A. Jensen. *Root cause defect identification in multicrystalline silicon for improved photovoltaic module reliability.* PhD thesis, Massachussets Institute of Tecnology, 6 2018.

[40] D. Bredemeier, D. Walter, S. Herlufsen, and J. Schmidt. Lifetime degradation and regeneration in multicrystalline silicon under illumination at elevated temperature. *AIP Advances*, 6(3):035119, 2016.

[41] C. E. Chan, D. N. R. Payne, B. J. Hallam, M. D. Abbott, T. H. Fung, A. M. Wenham, B. S. Tjahjono, and S. R. Wenham. Rapid stabilization of high-performance multicrystalline p-type silicon PERC cells. *IEEE Journal of Photovoltaics*, 6(6):1473–1479, 2016.

[42] A. Herguth, P. Keller, and N. Mundhaas. Influence of temperature on light induced phenomena in multicrystalline silicon. *AIP Conference Proceedings*, 1999(1):130007, 2018.

[43] F. Kersten, J. Heitmann, and J. W. Müller. Influence of Al2O3 and SiNx Passivation Layers on LeTID. *Energy Procedia*, 92:828–832, 2016.

[44] W. Eberle, R.and Kwapil, F. Schindler, M. C. Schubert, and S. W. Glunz. Impact of the firing temperature profile on light induced degradation of multicrystalline silicon. *physica status solidi (RRL) – Rapid Research Letters*, 10(12):861–865, 2016.

[45] D. Bredemeier, D. Walter, and J. Schmidt. Light-induced lifetime degradation in high-performance multicrystalline silicon: Detailed kinetics of the defect activation. *Solar Energy Materials and Solar Cells*, 173:2–5, 2017.

[46] S. Liu, C. Chan, D. Chen, M. Kim, C. Sen, U. Varshney, B. Hallam, M. Abbott, S. Wenham, and D. Payne. Investigation of temperature and illumination dependencies of carrier-induced degradation in p-type multi-crystalline silicon. *AIP Conference Proceedings*, 1999(1):130014, 2018.

[47] W. Kwapil, T. Niewelt, and M. C. Schubert. Kinetics of carrier-induced degradation at elevated temperature in multicrystalline silicon solar cells. *Solar Energy Materials and Solar Cells*, 173:80–84, 2017.

[48] J. Hofstetter, C. del Cañizo, H. Wagner, S. Castellanos, and T. Buonassisi. Material requirements for the adoption of unconventional silicon crystal and wafer growth techniques for high-efficiency solar cells. *Progress in Photovoltaics: Research and Applications*, 24(1):122–132, 2016.

[49] D. Bredemeier, D. C. Walter, and J. Schmidt. Lifetime degradation in multicrystalline silicon under illumination at elevated temperature: Indications for the involvement of hydrogen. *AIP Conference Proceedings*, 1999(1):130001, 2018.

[50] M. A. Jensen, A. E. Morishige, S. Chakraborty, R. Sharma, H. S. Laine, B. Lai, V. Rose, A. Youssef, E. E. Looney, S. Wieghold, J. R. Poindexter, J. Correa-Baena, T. Felisca, H. Savin, J. B. Li, and T. Buonassisi. Solubility and diffusivity: Important metrics in the search for the root cause of light- and elevated temperature-induced degradation. *IEEE Journal of Photovoltaics*, 8(2):448–455, 2018.

[51] C. Vargas, Y. Zhu, G. Coletti, C. Chan, D. Payne, M. Jensen, and Z. Hameiri. Recombination parameters of lifetime-limiting carrier-induced defects in multicrystalline silicon for solar cells. *Applied Physics Letters*, 110(9):092106, 2017.

[52] A. E. Morishige, M. A. Jensen, D. B. Needleman, K. Nakayashiki, J. Hofstetter, T. A. Li, and T. Buonassisi. Lifetime Spectroscopy Investigation of Light-Induced Degradation in p-type Multicrystalline Silicon PERC. *IEEE Journal of Photovoltaics*, 6(6):1466–1472, 2016.

[53] H. Deniz, J. Bauer, and O. Breitenstein. Nickel precipitation in light and elevated temperature degraded multicrystalline silicon solar cells. *Solar RRL*, 2(9):1800170, 2018.

[54] M. Wagner, F. Wolny, M. Hentsche, A. Krause, L.e Sylla, F. Kropfgans, M. Ernst, R. Zierer, P. Bönisch, P. Müller, N. Schmidt, V. Osinniy, H.-P. Hartmann, R. Mehnert, and H. Neuhaus. Correlation of the LeTID amplitude to the Aluminium bulk concentration and Oxygen precipitation in PERC solar cells. *Solar Energy Materials and Solar Cells*, 187:176–188, 2018.

[55] F. Kersten, P. Engelhart, H. C. Ploigt, F. Stenzel, K. Petter, T. Lindner, A. Szpeth, M. Bartzsch, A. Stekolnikov, M. Scherff, J. Heitmann, and J. W. Müller. A New Light Induced Volume Degradation Effect of mc-Si Solar Cells and Modules. In *31st EUPVSEC (WIP, Münich)*. WIP, 2015.

[56] K. Petter, K. Hübener, F. Kersten, M. Bartzsch, F. Fertig, and J. Müller. Dependence of LeTID on brick height for different wafer suppliers with several resistivities and dopants. In *9th International Workshop on Crystalline Silicon for Solar Cells*. WIP, 2016.

[57] D. Chung, C. Chan, B. Mitchell, P. P. Altermatt, T. Trupke, and M. Abbott. Effect of wafer position in ingot on the light and elevated temperature induced degradation (LeTID) of multicrystalline silicon. In *2018 IEEE 7th World Conference on Photovoltaic Energy Conversion (WCPEC) (A Joint Conference of 45th IEEE PVSC, 28th PVSEC & 34th EU PVSEC)*, pages 0303–0308, 2018.

[58] A. Inglese, A. Focareta, F. Schindler, J. Schön, J. Lindroos, M. C. Schubert, and H. Savin. Light-induced degradation in multicrystalline silicon: The role of copper. *Energy Procedia*, 92:808–814, 2016.

[59] J. Lindroos, Y. Boulfrad, M. Yli-Koski, and H. Savin. Preventing light-induced degradation in multicrystalline silicon. *Journal of Applied Physics*, 115(15):154902, 2014.

[60] J. Lindroos and H. Savin. Review of light-induced degradation in crystalline silicon solar cells. *Solar Energy Materials and Solar Cells*, 147:115–126, 2016.

[61] A. Schmid, A. Zuschlag, D. Skorka, J. Fritz, C. Winter, and G. Hahn. Influence of different transition metal contaminations on degradation and regeneration in mc-Si. In *33rd European Photovoltaic Solar Energy Conference and Exhibition*, pages 321–324, 2017.

[62] T. Niewelt, F. Schindler, W. Kwapil, R. Eberle, J. Schön, and M. C. Schubert. Understanding the light-induced degradation at elevated temperatures: Similarities between multicrystalline and floatzone p-type silicon. *Progress in Photovoltaics: Research and Applications*, 26(8):533–542, 2018.

[63] D. Bredemeier, D. C. Walter, R. Heller, and J. Schmidt. Impact of hydrogen-rich silicon nitride material properties on light-induced lifetime degradation in multicrystalline silicon. *physica status solidi (RRL) – Rapid Research Letters*, 13(8):1900201, 2019.

[64] M. S. Wiig, H. Haug, R. Søndenå, and E. S. Marstein. Modeling of recombination strength at grain boundaries after phosphorus diffusion gettering and the effect of hydrogen passivation. In *7th International Conference on Silicon Photovoltaics, SiliconPV 2017*, volume 124, pages 215–224, 2017.

[65] K. Adamczyk, R. Søndenå, C. C. You, G. Stokkan, J. Lindroos, M. Rinio, and M. Di Sabatino. Recombination strength of dislocations in high-performance

multicrystalline/quasi-mono hybrid wafers during solar cell processing. *physica status solidi (a)*, 215(2):1700493, 2018.

[66] T. H. Fung, M. Kim, D. Chen, C. E. Chan, B. J. Hallam, R. Chen, D. N. R. Payne, A. Ciesla, S. R. Wenham, and M. D. Abbott. A four-state kinetic model for the carrier-induced degradation in multicrystalline silicon: Introducing the reservoir state. *Solar Energy Materials and Solar Cells*, 184:48–56, 2018.

[67] D. N. R. Payne, C. E. Chan, B. J. Hallam, B. Hoex, M. D. Abbott, S. R. Wenham, and D. M. Bagnall. Acceleration and mitigation of carrier-induced degradation in p-type multi-crystalline silicon. *physica status solidi (RRL) – Rapid Research Letters*, 10(3):237–241, 2016.

[68] K. Krauss, A. A. Brand, F. Fertig, S. Rein, and J. Nekarda. Fast regeneration processes to avoid light-induced degradation in multicrystalline silicon solar cells. *IEEE Journal of Photovoltaics*, 6(6):1427–1431, 2016.

[69] A. Zuschlag, D. Skorka, and G. Hahn. Degradation and Regeneration in mc-Si After Different Gettering Steps. In *32nd European Photovoltaic Solar Energy Conference and Exhibition*. WIP, 2016.

[70] D. Chen, P. Hamer, M. Kim, C. Chan, A. Ciesla nee Wenham, F. Rougieux, Y. Zhang, M. Abbott, and B. Hallam. Hydrogen-induced degradation: Explaining the mechanism behind light- and elevated temperature-induced degradation in n- and p-type silicon. *Solar Energy Materials and Solar Cells*, 207, 2020.

[71] C. Zhou, F. Ji, S. Cheng, J. Zhu, W. Wang, and D. Hu. Light and elevated temperature induced degradation in B–Ga co-doped cast mono Si PERC solar cells. *Solar Energy Materials and Solar Cells*, 211, 2020.

[72] M. Syre, S. Karazhanov, B. R. Olaisen, A. Holt, and B. G. Svensson. Evaluation of possible mechanisms behind p gettering of iron. *Journal of Applied Physics*, 110(2):024912, 2011.

[73] S. Gindner, P. Karzel, B. Herzog, and G. Hahn. Efficacy of phosphorus gettering and hydrogenation in multicrystalline silicon. *IEEE Journal of Photovoltaics*, 4(4):1063–1070, 2014.

[74] A. A. Istratov, T. Buonassisi, R. J. McDonald, A. R. Smith, R. Schindler, J. A. Rand, J. P. Kalejs, and E. R. Weber. Metal content of multicrystalline silicon for solar cells and its impact on minority carrier diffusion length. *Journal of Applied Physics*, 94(10):6552–6559, 2003.

[75] B.L. Sopori, X. Deng, J.P. Benner, A. Rohatgi, P. Sana, S.K. Estreicher, Y.K. Park, and M.A. Roberson. Hydrogen in silicon: A discussion of diffusion and passivation mechanisms. *Solar Energy Materials and Solar Cells*, 41-42:159 – 169, 1996.

[76] R. A. Sinton, A. Cuevas, and M. Stuckings. Quasi-steady-state photoconductance, a new method for solar cell material and device characterization. *25th IEEE Photovoltaic Specialists Conference*, pages 457–460, 1996.

[77] R. A. Sinton and A. Cuevas. Contactless determination of current–voltage characteristics and minority-carrier lifetimes in semiconductors from quasi-steady-state photoconductance data. *Applied Physics Letters*, 69(17):2510–2512, 1996.

[78] H. Nagel, C. Berge, and A. G. Aberle. Generalized analysis of quasi-steady-state and quasi-transient measurements of carrier lifetimes in semiconductors. *Journal of Applied Physics*, 86(11):6218–6221, 1999.

[79] H. Sio, S. Phang, P. Zheng, Q. Wang, H. Chen, W.and Jin, and D. Macdonald. Recombination sources in p-type high performance multicrystalline silicon. *Japanese Journal of Applied Physics*, 56(8):08MB16, 2017.

[80] T. Trupke, R. A. Bardos, M. D. Abbott, F. W. Chen, J. E. Cotter, and A. Lorenz. Fast photoluminescence imaging of silicon wafers. In *World Conference on Photovoltaic Energy Conversion*, Waikoloa, HI, USA, 2006.

[81] T. Trupke, R. A. Bardos, M. C. Schubert, and W. Warta. Photoluminescence imaging of silicon wafers. *Applied Physics Letters*, 89(044107), 2006.

[82] T. Trupke, B. Mitchell, J. W. Weber, W. McMillan, R. A. Bardos, and R. Kroeze. Photoluminescence imaging for photovoltaic applications. *Energy Procedia*, 15:135–146, 2012.

[83] S. Herlufsen, J. Schmidt, D. Hinken, K. Bothe, and R. Brendel. Photoconductance-calibrated photoluminescence lifetime imaging of crystalline silicon. *Physica Status Solidi Rapid Research Letters*, 2(6):245–247, Dec 2008.

[84] J. Haunschild, I. E. Reis, T. Chipei, M. Demant, B. Thaidigsmann, M. Linse, and S. Rein. Rating and sorting of mc-Si as-cut wafers in solar cell production using PL imaging. *Solar Energy Materials and Solar Cells*, 106:71–75, 2012.

[85] International Electrochemical Commission. IEC 60904-3: PV devices – Part 3: Measurement principles for terrestrial photovoltaic (PV) devices with reference spectral irradiance data.

[86] A. Herguth. On the meaning(fullness) of the intensity unit ‘suns’ in light induced degradation experiments. *Energy Procedia*, 124:53–59, 2017.

[87] J. Isenberg, J. Dicker, and W. Warta. Averaging of laterally inhomogeneous lifetimes for one-dimensional modeling of solar cells. *Journal of Applied Physics*, 94(6):4122–4130, 2003.

[88] H. C. Sio, A. Fell, S. P. Phang, H. Wang, P. Zheng, D. K. Chen, X. Zhang, T. Zhang, H. Jin, and D. Macdonald. 3-D Modeling of Multicrystalline Silicon Materials and Solar Cells. *IEEE Journal of Photovoltaics*, 9(4):965–973, 2019.

[89] A. Herguth. On the lifetime-equivalent defect density: Properties, application, and pitfalls. *IEEE Journal of Photovoltaics*, 9(5):1182–1194, 2019.

[90] F. D. Heinz, Y. Zhu, Z. Hameiri, M. Juhl, T. Trupke, and M. C. Schubert. The principle of adaptive excitation for photoluminescence imaging of silicon: Theory. *physica status solidi (RRL) – Rapid Research Letters*, 12(7):1800137, 2018.

[91] P. Virtanen, R. Gommers, T. E. Oliphant, M. Haberland, T. Reddy, E. Cournapeau, D.and Burovski, P. Peterson, W. Weckesser, J. Bright, S. J. van der Walt, M. Brett, J. Wilson, K. Jarrod Millman, A. R. J. Mayorov, N.and Nelson, E. Jones, R. Kern, E. Larson, CJ Carey, İ. Polat, Y. Feng, E. W. Moore, J. Vand erPlas, D. Laxalde, J. Perktold, R. Cimrman, I. Henriksen, E. A. Quintero, C. R Harris, A. M. Archibald, A. H. Ribeiro, F. Pedregosa, P. van Mulbregt, and SciPy 1. 0 Contributors. SciPy 1.0: Fundamental Algorithms for Scientific Computing in Python. *Nature Methods*, 17:261–272, 2020.

[92] I. R. Gatland and W. J. Thompson. A weight-watcher's guide to least-squares fitting. *Computers in Physics*, 7(3):280–285, 1993.

[93] S. Liu, D. Payne, C. Vargas, D. Chen, M. Kim, C. Sen, U. Varshney, Z. Hameiri, C. Chan, and S. Abbott, M.and Wenham. Impact of dark annealing on the kinetics of light- and elevated-temperature-induced degradation. *IEEE Journal of Photovoltaics*, 8(6):1494–1502, 2018.

[94] T. Luka, M. Turek, and C. Hagendorf. Defect formation under high temperature dark-annealing compared to elevated temperature light soaking. *Solar Energy Materials and Solar Cells*, 187:194–198, 2018.

[95] T. Niewelt, R. Post, F. Schindler, W. Kwapil, and M. C. Schubert. Investigation of LeTID where we can control it – Application of FZ silicon for defect studies. *AIP Conference Proceedings*, 2147(1):140006, 2019.

[96] D. V. Lang and L. C. Kimerling. Observation of recombination-enhanced defect reactions in semiconductors. *Phys. Rev. Lett.*, 33:489–492, Aug 1974.

[97] L.C. Kimerling. Recombination enhanced defect reactions. *Solid-State Electronics*, 21(11):1391 – 1401, 1978.

[98] H. Sumi. Dynamic defect reactions induced by multiphonon nonradiative recombination of injected carriers at deep levels in semiconductors. *Phys. Rev. B*, 29:4616–4630, Apr 1984.

Master's thesis

2020

Ida Due-Sørensen

NTNU
Norwegian University of
Science and Technology

IFE